

Interneuron diversity in the human dorsal striatum

Leonardo Garma

Karolinska Institutet

Lisbeth Harder

Karolinska Institutet

Juan Barba-Reyes

University of Cadiz

Monica Diez-Salguero

University of Cadiz

Alberto Serrano-Pozo

Massachusetts General Hospital, Harvard Medical School <https://orcid.org/0000-0003-0899-7530>

Bradley Hyman

Massachusetts General Hospital, Harvard Medical School <https://orcid.org/0000-0002-7959-9401>

Ana Munoz-Manchado (✉ ana.munoz@uca.es)

University of Cadiz <https://orcid.org/0000-0002-1121-6072>

Article

Keywords:

Posted Date: May 24th, 2023

DOI: <https://doi.org/10.21203/rs.3.rs-2921627/v1>

License: © ⓘ This work is licensed under a Creative Commons Attribution 4.0 International License.

[Read Full License](#)

Abstract

Deciphering the striatal interneuron diversity is key to understanding the basal ganglia circuit and to untangle the complex neurological and psychiatric diseases affecting this brain structure. We performed snRNA-seq of postmortem human caudate nucleus and putamen samples to elucidate the diversity and abundance of interneuron populations and their transcriptional structure in the human dorsal striatum. We propose a new taxonomy of striatal interneurons with eight main classes and fourteen subclasses and provide their specific markers and some quantitative FISH validation, particularly for a novel PTHLH-expressing population. For the most abundant populations, PTHLH and TAC3, we found matching known mouse interneuron populations based on key functional genes such as ion channels and synaptic receptors. Remarkably, human TAC3 and mouse Th populations share important similarities including the expression of the neuropeptide tachykinin 3. Finally, we were able to integrate other published datasets supporting the generalizability of this new harmonized taxonomy.

Introduction

The dorsal striatum is a subcortical brain structure that in human consists of caudate nucleus (CN) and putamen (Pu), separated by the internal capsule. Together with the ventral striatum (nucleus accumbens and olfactory tubercle), the globus pallidus, the subthalamic nucleus, and the substantia nigra, it makes up the basal ganglia nuclei¹. The striatum carries out functions related to motor control, action learning, reward-related behavior, and cognition with certain regional preferences. The CN is mainly responsible for eye movement and cognitive functions, the Pu for motor control, learning, and auditory responses, and the ventral striatum is related to limbic functions such as reward and motivation. Dysfunction of the striatum is a key feature of neurodegenerative disorders such as Parkinson's and Huntington's diseases^{2,3,4,5} as well as of psychiatric conditions such as obsessive-compulsive disorder and schizophrenia^{6,7,8}.

The dorsal striatum is the main input area of the basal ganglia and exhibits a high level of activity-dependent synaptic plasticity⁹, representing a critical hub for the process and selection of information sent to the other basal ganglia nuclei. This information is relayed through the projecting neurons, known as medium spiny neurons (MSNs) because of their morphological features¹⁰. MSNs, which are characterized by their inhibitory signaling via gamma-aminobutyric acid (GABA), constitute the majority of the striatal neuronal population. However, their function depends on a diverse group of locally-projecting neurons known as interneurons.

Striatal interneurons integrate incoming information from different brain areas and act on MSNs activity to modulate the output information. This filtering process is also regulated by incoming dopaminergic and serotonergic projections from the midbrain and the dorsal raphe nucleus, respectively^{11,12}. The spiny striatal interneurons have been classically differentiated into two main groups: a small group of cholinergic giant neurons and a diverse population of GABAergic medium-size neurons, based on a variety of specific markers and electrophysiological profiles^{13,14,15}. Since the striatal interneurons have

received little attention compared to the MSNs, consensus regarding the populations comprising these neuronal groups and how to identify them is lacking. However, recent advances such as new transgenic reporter mice that target the complete striatal and cortical interneuron repertoire^{15,16}, and single cell/nucleus RNA-sequencing (sc/nRNA-seq) have enabled large-scale approaches to investigate cell diversity based on the individual cell transcriptome^{17,18,19} in different mouse brain areas including the striatum^{20,21,22}. Using these methods, a recent study identified seven interneuron populations in the mouse striatum based on their molecular and electrophysiological profile: Npy/Sst, Npy/Mia, Cck/Vip, Cck, Chat, Th, and Pthlh²⁰. Among them the *Pthlh*-expressing interneurons represent a novel class of striatal interneurons that is characterized by a variable *Pvalb* expression level and a broad continuum of intrinsic electrophysiological properties, which correlates with *Pvalb* levels²⁰. This continuum seems to follow a regional gradient pattern within the mouse dorsal striatum suggesting that the different types of striatal cells receive inputs from different brain cortical areas²³.

Nevertheless, interneuron diversity in the human CN and Pu in terms of abundance and molecular identity remains unsolved. Most of the studies are limited by the technical approach because they have relied on the classical markers to identify interneuron populations and focused primarily on the cholinergic cells, expressing choline acetyltransferase (ChAT)^{24,25,26}. Prior snRNA-seq studies on the human and non-human primate striatum have highlighted different aspects, such as broad differences across species and brain areas^{27,28} or in health vs. disease²⁹, but lack sufficient interneuron sampling to characterize striatal interneuron diversity. In the present study, we have used snRNA-seq to investigate the diversity of interneurons on the human dorsal striatum (CN and Pu) from a total of 28 donors. Our sampling comprises nearly half a million nuclei overall, which constitutes by far the largest study of this kind to date. We have leveraged this large dataset to establish the major and minor divisions between the interneuron classes and types in both regions and provide specific markers for each. We have validated part of our classification in tissue sections, confirming novel populations and markers (such as PTHLH, PVALB, and DACH1), identified differences between CN and Pu, and demonstrated an internal gradient structure within cell subclasses. Moreover, we have discovered key synapse-related genes in our taxonomy and described a consistent link between mouse and human PTHLH and TAC3 classes. Our taxonomy resisted the test of comparison with prior human striatal snRNA-seq datasets, supporting our taxonomy as a valid consensus classification of striatal interneurons.

Results

Interneuron heterogeneity in the human dorsal striatum

With the objective to further decode the diversity of interneurons in the human dorsal striatum, we isolated and sequenced single nuclei from fresh frozen CN (N = 25) and Pu (N = 28) samples of 28 control donors that did not meet diagnostic criteria for any neurodegenerative disease (Supplementary table 1). Samples were processed using an established snRNA-seq workflow, which allowed the enrichment of neuronal population by applying fluorescent-activated nuclei sorting. A subset of six Pu samples was

additionally utilized in high-sensitivity fluorescent *in situ* hybridization (FISH) experiments to validate RNA expression patterns in tissue sections (Fig. 1A).

The sequencing yielded 455,886 nuclei, out of which we discarded 29.4% after a thorough quality control process (Supplementary Fig. 1). From the remaining nuclei, we selected the interneurons through an iterative classification process in which we discarded glial cells, MSNs, and excitatory neurons based on bona-fide markers—astrocytes (*AQP4*, *ADGRV1*), microglia (*CSF1R*, *FYB1*), oligodendrocytes (*MBP*, *MOG*, *MAG*), oligodendrocyte precursor cells (*PTPRZ1*, *PDGFRA*, *VCAM*), vascular cells (*EBF1*, *ABCB1*, *ABCA9*), MSNs (*PPP1R1B*, *DRD1*, *DRD2*), and excitatory neurons (*SLC17A7*)—and selected positively for nuclei expressing *GAD1* and/or *GAD2*. This classification process resulted in **19,339** nuclei labeled as interneurons, representing the largest dataset of human interneurons from the dorsal striatum available to date. The interneuron populations represented **10.67%** of the total neuronal cells.

After clustering the data, we identified eight main interneuron classes: CCK/VIP (*ADARB2+*, *CCK+*, and *VIP+*), CCK (*ADARB2+* and *CCK+*), PVALB (*PVALB+*), SST/GRIK3 (*SST+* and *GRIK3+*), SST/NPY (*SST+* and *NPY+*), PTHLH (*PTHLH+* and *OPN3+*), CHAT (*CHAT+* and *SLC5A7+*) and TAC3 (*TAC3+* and *PTPRK+*) (Fig. 1B), which could be divided into fourteen different subclasses identified by unique transcriptomic patterns (Fig. 1C, D). The complete results of a differential expression analysis at class and subclass levels are provided in Supplementary table 2.

In our dataset, PTHLH and TAC3 constitute the largest interneuron classes, accounting for 28% and 28.6% of all detected interneurons, respectively. Both PTHLH and TAC3 contained small subclasses, distinguishable from the main type by the expression of *MOXD1* and *SEMA3A*, respectively. The *ADARB2+* population (CCK and CCK/VIP classes) was equally abundant (28.1% of all interneurons) but exhibited a higher heterogeneity, with four subclasses clearly differentiated by specific marker genes. Although we followed the classical division between CCK and CCK/VIP, we observed that the *ADARB2+* neurons could also be divided by the expression of the chemokine ligand *CXCL14* and the cadherin *CDH10* (Supplementary Fig. 2). We also found a great diversity of transcriptomic profiles among the neurons expressing *PVALB* and *SST*, as these two classes could be divided into five different subclasses based on the expression levels of two novel marker genes: *GRIK3*, which encodes the Glutamate Ionotropic Receptor Subunit 3, and *DACH1*, which encodes the Dachshund Family Transcription Factor 1. These five subclasses together represent 15% of the total of interneurons.

Interestingly, we also found a smattering of TAC3 expression in the CCK and CCK/VIP populations, therefore the TAC3 population is best defined by its high expression level of *PTPRK* (protein tyrosine phosphatase receptor type K). Similarly, we also noted low levels of *OPN3* (Opin3)—one of the marker genes of the PTHLH cells—in the CCK and CCK/VIP populations.

Validation of interneuron taxonomy with fluorescent in situ hybridization

The magnitude of the snRNA-seq dataset produced in the present study allowed us to detect novel interneuron populations with distinct transcriptomic profiles (Fig. 1C, D). Therefore, we sought to validate

some of these subclasses through quantitative multiplex FISH using up to three marker genes. Using probes against *SST*, *NPY* and *DACH1*, we were able to detect cells double-positive for *SST* and *NPY* in the Pu of all six donors assayed; the same applied to cells triple-positive for *SST*, *NPY*, and *DACH1* (Fig. 2B-D). This is in line with our sequencing data (Fig. 2A) and supports our decision to split the main class of *SST*/*NPY* interneurons into the *SST*/*NPY* and *SST*/*NPY*/*DACH1* subclasses. In addition, in this FISH we identified a group of cells that were only positive for *SST* and most likely correspond to the subclass *SST*/*GRIK3*. The most conspicuous group of cells in this FISH was only positive for *DACH1*, which cannot be explained by the low *DACH1* expression found in *CCK*/*VIP* and *PVALB*/*GRIK3* subclasses alone (Fig. 2A); however, an extended search for *DACH1* expression in our dataset revealed that MSNs, as well as some astrocytes, endothelial cells, and pericytes are positive for this marker (data not shown).

PVALB-expressing interneuron subclasses are of particular interest because *PVALB* has traditionally been used to identify a class of striatal interneurons. In contrast to the mouse striatum, in which *Pvalb*+ interneurons have been described to be contained within the *Pthlh*+ cells²⁰ (i.e., all *Pvalb*+ interneurons are *Pthlh*+), our snRNA-seq data from human CN and Pu indicates the presence of a distinct *PVALB* positive but *PTHLH* negative subclass of interneurons. FISH using *PTHLH* and *PVALB* probes revealed *PTHLH* single-positive cells as well as *PTHLH* and *PVALB* double-positive cells in all six donors analyzed while *PVALB* single-positive cells were found in five of the six donors (Fig. 2E). For both single-positive groups, the number of detected cells was highly variable across donors, while double-positive cells occurred in low numbers in all of them. Thus, while this experiment proves that *PTHLH* and *PVALB* double-positive cells exist in both human and mouse dorsal striatum, we provide evidence of a group of *PVALB* interneurons expressing minimal or no *PTHLH* at all in the human dorsal striatum (Fig. 2A and 2G).

Interneuron populations exhibit region-based differences within the striatum

While we found all the interneuron classes identified in our snRNA-seq data in both the CN and the Pu (Fig. 3A), we did note slight differences in abundance between both regions: CN was significantly richer in *PTHLH* interneurons (35.6% vs. 20.3%, p-value = 0.001), whereas the *CCK*, *SST*/*GRIK3* and *PVALB* classes were significantly more abundant in the Pu (12.1% vs. 7.1%, 3.5% vs. 2.4%, and 5.5% vs. 2.7%, respectively, with the belonging p-values in the same order 0.008, 0.027 and 0.015; Fig. 3C). Several interneuron classes also exhibited distinct region-dependent transcriptomic signatures. Most notably, we found that the *PTHLH* class had significant differences in the expression of 276 genes by region (i.e., 126 upregulated and 150 downregulated in CN vs. Pu). *SST*/*NPY*, *CHAT*, *TAC3*, and *CCK*/*VIP* classes also showed expression differences in CN vs. Pu, but of smaller magnitude (Fig. 3B, Supplementary table 3).

To contextualize the changes in expression of the *PTHLH* class neurons across the two striatal regions, we conducted a gene-set enrichment analysis using the genes significantly upregulated in either region (Fig. 3D). The 126 genes upregulated in the CN were enriched in GO-terms associated with secretory vesicles and their transport, whereas the 150 genes with significantly higher expression in the Pu were

enriched in GO-terms associated with receptor complexes, ion channel complexes, plasma membrane components, and G-protein-coupled receptor activity (GPCR). This signal transduction via GPCRs relies upon the production of cAMP and other signaling cascades³⁰. KEGG pathways showed that the differentially upregulated genes in Pu are related to the cAMP signaling pathway, including genes such as *ADCY8* (GPCR), *CRHR1*, *GRIA3*, *GRIN3A*, *PDE4B*, *PLCE1*, and *RYR2*. Thus, these data suggest that there is an over-expression of AMPA and NMDA receptor subunits (related to Ca²⁺ + and Na⁺ flux) in Pu compared to CN via cAMP/GPCRs activation, which could lead to enhanced long-term potentiation and higher synaptic plasticity in Pu vs. CN and explain why CN and Pu inputs and functionalities are not equivalent³¹.

PTHLH and TAC3 subclasses exhibit changes along continuous transcriptomic profiles

Our initial cluster analysis allowed us to detect fourteen different interneuron subclasses, each characterized by the expression of a unique combination of marker genes. However, previous studies have shown that striatal interneurons display gene expression gradients^{20,21,22} and, therefore, their diversity may not be captured by oversimplistic binary classifications. To investigate if this phenomenon was observable in our dataset, we conducted a factor analysis within the largest subclasses (PTHLH and TAC3) on each striatal region. In both subclasses and regions, the factor analysis revealed coordinated gradual changes of sets of genes (Fig. 4A to D, left and middle panels). The genes with the highest weights on the factor describing the differences within each population were different across regions (Fig. 4A to D, right panel, Supplementary table 4), although there were some commonalities; for example, large changes in *SLIT1*, *CNTN5*, and *TAF A2* expression were observed in the PTHLH neurons in both Pu and CN. Similarly, *KCNIP4*, *ASIC2*, and *MARCH1* were responsible for some of the largest variations across the TAC3 neurons in both striatal regions. Notably, some of the genes with the greatest contributions to the intra-subclass variance (*KCNIP4*, *ASIC2*, *RYR2*) are ion channel subunits, suggesting the possible existence of different electrophysiological phenotypes within the same transcriptomic subclass. To gain a better understanding of the differences revealed by the factor analysis, we conducted a gene set enrichment analysis on the genes with the largest contributions to the factor on each case (Supplementary Figs. 3 and 4).

TAC3 genes associated with the gradient driven by *KCNIP4* and *ASIC2* expression levels showed similar enriched terms in both CN and Pu (Supplementary Fig. 4). Relevant terms were mostly related to the regulation of synapse formation or activity and cell adhesion. PTHLH genes related to the gradient driven by *GULP1*, *ZNF385D*, and *RYR2* expression levels in the CN (*CDH8*, *PDE4B*, and *FRAS1* in Pu) displayed terms linked to cell adhesion and channel complexes, specifically Ca²⁺ channels (Supplementary Fig. 3). However, results for genes from the Pu gradient defined by *CNTN5*, *TAF A2*, and *SLIT1* showed biological specificity: GO-term enrichment analysis uncovered functionalities in synapse organization and ion transporter activity via ion channels that appear to be specific to the Pu.

Interneuron taxonomy is maintained across functionally relevant genes

To understand the potential functional implications of our taxonomy, we investigated the differences existing between the established subclasses across two separate sets of genes highly relevant to neuronal function. First, we restricted our dataset to the genes corresponding to dopamine, GABA, acetylcholine, and glutamate receptors. The UMAP projection of our data on this set of genes shows a clear separation between the different subclasses (Fig. 5A, left) and the differential expression analysis revealed unique neurotransmitter-receptor expression patterns (Supplementary Fig. 5, Supplementary table 5). Markers fitting this pattern noteworthy were: *GRIN3A* and *GRM5* in CCK interneuron class; *GRM7*, *CHRM3*, *GABRA1*, and *CHRNA2* in CCK/VIP; *GRIN2C* in PVALB; *GRIK3*, *GRIK1*, *GRM1*, and *GRIK1* in SST/GRIK3; *GRIP1* and *GRIA4* in PTHLH; *TRPC3* in CHAT; and *GRM8*, *GRID1*, *CHRM2*, and *CHRNA7* in TAC3 interneurons.

We conducted a similar analysis using all the genes under the GO-term “ion channel activity” (GO:0005216). The UMAP projection of the data using only ion channels retained the separation between subclasses (Fig. 5A, right), whereas the differential expression analysis rendered unique transcriptomic patterns. Relevant markers related to these patterns were: *KCNIP1*, *CACNA2D1*, and *KCNH5* in CCK; *GLRA2* and *KCNT2* in CCK/VIP; *KCNMB4* and *RYR1* in PVALB; *GRID2* in SST/GRIK3; *KCNMA1*, *GLRA3*, and *ITPR2* in PTHLH; *TRPC3* and *KCNG3* in CHAT; and *GRID1*, *SCN7A*, and *CACNA2D3* in TAC3 interneurons (Supplementary Fig. 5, Supplementary table 5).

A closer inspection of this functional analysis revealed a strong parallelism in key feature genes between the TAC3 population, recently described as a primate-specific class²⁷ and that we have thoroughly characterized in the present work, and the mouse interneuron Th cell class^{20,14}. Indeed, we found notable expression similarities when comparing the TAC3 human class presented here with the Th mouse class from dataset A in Ref.²⁰. Both classes share the expression of the Tachykinin precursor—*TAC3* in human and the homologous gene *Tac2* in mouse—and the *TRH* (Thyrotropin Releasing Hormone)—recently described as a marker for the mouse Th population²⁰. Additionally, they share the cholinergic nicotinic receptor subunits *CHRNA3/Chrna3* and *CHRN4/Chrn4*, the GDNF receptor *GFRA2/Gfra2*, and the prolactin receptor *PRLR/Prlr*. Interestingly, they also match in their negative expression patterns, such as the absence of expression of both Synaptotagmin 1 *SYT1/Syt1* and the glutamatergic receptor *GRIK1/Grik1*, which are remarkably highly expressed in the rest of interneuron populations in both human and mouse (Fig. 5B). Of note, in agreement with another study in the human striatum²⁷, we hardly detected any *TH* expression in the human interneuron populations, but we found it in MSNs (data not shown).

To determine the drive of the expression of ion channels in these interneuron subclasses, we focused on the typical genes of a Fast Spiking (FS) profile characteristic of high *PVALB*-expressing cells (Fig. 5C). This analysis showed significant expression of FS genes^{32,33–35} such as *KCNAB1* (Kvb1.3), *KCNC2*

(Kv3.2), *KCNA2* (Kv1.2), *KCNC1* (Kv3.1), *HCN1*, and *SCN1A* (Nav1.1) in PTHLH and PVALB cells, with a substantial overexpression in the latter (Fig. 5C). In the mouse *Pthlh* population, the FS profile correlated positively with the *Pvalb* expression level following a continuous gradient pattern Ref²⁰. Interestingly, in the human striatum, we also found a defined PVALB class of interneurons with high expression of the genes involved in the FS profile.

Interneuron taxonomy is consistent across published human striatal snRNAseq datasets

To further validate our findings and our classification of interneuron subclasses in the human striatum, we integrated our labeled data with four other datasets from three sources²⁷⁻²⁹ using scVI³⁶. These datasets included CN^{27,29}, Pu²⁹, and Nucleus Accumbens²⁸ human samples (Supplementary table 6). We filtered and normalized the raw counts from these four datasets and selected the interneuron nuclei based on the same markers as in our own dataset (see Methods). This resulted in a total of 8,090 additional interneuron nuclei added to our 19,339. We reduced the ensemble of the 5 datasets to the 12,986 overlapping genes, of which we selected the top 1,200 most variable to build an integrated model using scVI³⁶.

Remarkably, the UMAP projection of the integrated data revealed extensive overlap between nuclei from different datasets, indicating that the scVI model compensated possible batch-specific differences (Fig. 6A). Clustering the integrated data resulted in 16 groups (Fig. 6B), out of which 15 had a clear correspondence to our original interneuron subclass labels (Fig. 6C). Only cluster number 12 contained less than 1% of nuclei from our dataset and could not be readily matched to any of the described subclasses. This cluster consisted of 550 nuclei (2% of the total), 83.6% of which belonged to the DropSeq dataset from Krienen et al.'s study²⁷. To ensure that cells clustering together actually shared the same transcriptomic profile, we examined the expression of the subclass marker genes on each of the public datasets (Fig. 6D, Supplementary Fig. 6). As the figure shows, cells within the same cluster have similar expression patterns, which in turn correspond to one of the subclasses established in our taxonomy. In the case of cluster number 12, we observed that it did express the markers corresponding to our TAC3 subclass. Although there was a bias by dataset in some of the clusters, all contained nuclei from at least two different datasets, supporting the generalizability of our taxonomy (Fig. 6E).

Discussion

The neuronal communication in the striatum, a hub for motor and cognitive information, is modulated by the interneurons. Characterizing the diversity and abundance of these locally-projecting neurons is key to understand the proper functionality of this brain structure. Here we produced the largest snRNA-seq dataset of the human dorsal striatum (both in number of nuclei isolated and human samples) to date to profile the interneuron diversity of this brain structure (CN and Pu). We leveraged this dataset to perform a deep molecular characterization of the fourteen interneuron subclasses identified, provide a full set of marker genes for each one, and delineate functional aspects such as synapses-related machinery for

different classes, differences between CN and Pu, inner gradient structure of gene expression levels, and relevant pathways related to the main genetic differences.

Interneuron diversity in the human striatum is higher than expected

The interneuron diversity of the mammalian striatum has received little attention until recently, especially if we compare it with other brain regions, such as the cortex, where numerous investigations have been carried out³⁷. Classically, striatal interneurons have been identified according to five main markers: Calretinin (CR or CALB2), Tyrosine Hydroxylase (TH), Parvalbumin (PVALB), Choline acetyltransferase (CHAT), and Neuropeptide Y (NPY)^{38,39,24,40}.

With the development of snRNA-seq, many studies have contributed to elucidate the cellular composition of different brain areas, including the striatum, especially in the mouse brain. This technology offers a full genetic delineation to characterize molecular cell identities. Only a few published snRNA-seq datasets contain information regarding the human striatum, but they included a low number of interneurons and/or focused on other cell types, thus precluding the establishment of a comprehensive taxonomy, as suggested by their lack of agreement²⁷⁻²⁹. In this work, we have sampled nearly half a million CN and Pu nuclei, obtaining almost 20,000 high quality interneuron nuclei after a strict quality control and classification process, a number that enabled us to establish a new taxonomy of human striatal interneurons.

We found eight main classes that we named after one or two of their main molecular markers. Two of these eight main classes express *CCK* and represent almost one third of the total interneuron population. These two *CCK*+ populations were split into two subclasses: *CCK/VIP* and *CCK/VIP/CXCL14* for the ones expressing *VIP* and *CCK*, and *CCK* and *CCK/CHST9* for the ones that do not, respectively. Of note, they all share the expression of *ADARB2*, which separates them from the rest of interneurons and is a marker used to designate development origin from the caudal ganglionic eminence (CGE) of cortical interneurons⁴¹. Pertinent investigations would be needed to confirm whether this is also the case in striatum since cortex and striatum seem to present differences in the combinatorial markers of developmental origin^{42,43}. *CCK* and *CCK/VIP* populations were first reported as striatal interneuron cell class in a scRNA-seq study of the mouse striatum enriched for interneurons²⁰. *Adarb2/Cck* and *Adarb2/Vip* expressing interneurons have also been described in the striatum of marmoset and mouse in a cross-species study²⁷. Remarkably, we find an important increase of *CCK*-expressing cells in human vs. mouse dorsal striatum, which might indicate its greater involvement in highly complex computational processes for motor and cognitive functions in the human. Little is known about the role of *CCK*-expressing cells in the central nervous system⁴⁴, although *CCK* is widely used as an interneuron marker in cortical areas. Further investigations would be needed to decipher the role of one of the most abundant interneuron classes in the human striatum.

The hierarchical clustering of subclasses in our taxonomy places the *CCK*-expressing cells in the same main branch as a group of cells expressing the glutamatergic receptor subunit *GRIK3*. These can be divided into three main classes: PVALB, SST/*GRIK3*, and SST/*NPY*. The PVALB class further splits into a small population that does not express *GRIK3* (the only ones) and a larger PVALB/*GRIK3* population, which represents most cells with a high expression of *PVALB*. Intriguingly, SST/*GRIK3* cells are transcriptomically more similar to the *PVALB*+ populations than to the other *SST* expressing cells, which also express *NPY*. The SST/*NPY* interneurons, one of the classical groups, can be divided by the presence or absence of *DACH1*, which is highly relevant during human neurodevelopment. In the striatum *DACH1* has been described as co-expressed with *SST* as well as several MSN markers⁴⁵. Accordingly, we also observed *DACH1* expression in human striatal MSNs in adulthood (data not shown).

In the other branch of our classification, we find the two populations representing the most abundant interneuron classes: PTHLH and TAC3. Together with these classes, the well-described and scarce cholinergic cells (*CHAT*), which have already been thoroughly characterized in the literature^{3,25,46,47}. Both PTHLH and TAC3 populations further split into two subclasses of unequal proportions: PTHLH and PTHLH/*MOXD1*, and TAC3 and TAC3/*SEMA3A*, respectively.

A *PTHLH*+ population was first described in the mouse striatum²⁰, where it was characterized as a group of cells that expressed *Pvalb* in a gradient manner that correlated with their electrophysiological properties, spatial distribution, morphology, and long-range inputs²³. In the human striatum this population is characterized by the expression of *OPN3*, *IL1RAPL2*, and *THSD4*, and shows a higher abundance in the CN than in the Pu. A PTHLH subclass shows specific expression of *MOXD1*—a monooxygenase predicted to be involved in the dopamine catabolic process—suggesting dopaminergic modulation by these cells. Similarly, to the mouse striatum, we find *PVALB* expression in the PTHLH population. This *PTHLH*+/*PVALB*+ population has also been confirmed by others in the striatum of the human as well as other species such as the marmoset and the mouse amygdala²⁷, <https://www.biorxiv.org/content/10.1101/2022.10.25.513733v1>. Interestingly, we have found a specific and less abundant class that expresses *PVALB* (at a significantly higher level than the PTHLH/*PALB* cells) but not *PTHLH*. This finding was validated with FISH and differs from the mouse striatum, where all *Pvalb*-expressing cells were also *Pthlh*+. These two classes, PTHLH and PVALB, do not appear close in their molecular identities in the human striatum when applying unbiased hierarchical clustering; however, when we performed a hypothesis-driven analysis of our data, restricted to relevant genes for neuronal functions such as neurotransmitter receptors or ion channels, these two classes showed a very strong correlation. This suggests that even though their overall molecular identities are far apart, these two classes might share functional roles in the striatal circuit. This observation brings up the recurrent debate on what constitutes a cell class^{48–51} and, more importantly, indicates that examining specific aspects of cell identity will deliver different pieces of information, such as what other cell(s) they communicate with and what kind of electrical activity they present. With that framework in mind, we also analyzed the most relevant genes for FS activity, characteristic of high *Pvalb*-expressing cells in the mouse striatum. Our

data showed that in the human striatum, all the FS relevant genes presented higher expression levels in both PTHLH and PVALB classes, but substantially higher in the latter.

TAC3 was recently described as a primate-specific striatal population²⁷. We did define a population of interneurons with high *TAC3* expression as the TAC3 class. However, this class was best defined by the expression of *PTPRK*, *TMEM163*, and *GFRA2* since *TAC3* is also expressed by the CCK/VIP class, a co-expression that was also reported by Krienen et al.²⁷. Through our functional gene analysis, we observed that TAC3 is characterized by synaptic receptors for glutamate (*GRM8*) and acetylcholine muscarinic (*CHRM2*) as well as nicotinic (*CHRNA7*, *CHRNB4*) receptors. Among the genes with ion channel activity, we found *GRID1* (glutamate ionotropic receptor), *SCN7A* (sodium voltage-gated channel), and *CACNA2D3* (Calcium Voltage-gated channel). Interestingly, when comparing functional genes in human vs. mouse striatum²⁰, we found that the mouse interneuron Th cell class had been previously described to express nicotinic receptors, including those responding to $\alpha 3\beta 4$ (a specific subtype)^{47,52,53}. This mouse Th population is characterized by the expression of *Tac2* (homologous of the human *TAC3* gene coding for a tachykinin precursor) and also by the expression of *Trh*, which is one of the best markers for Th cells in mouse. Remarkably, both populations share a specific pattern expression for *PRLR* (prolactin receptor), *GFRA2* (GDNF receptor), *SYT1* (synaptotagmin), and *GRIK1* (Glutamate ionotropic receptor subunit). For the last two genes (*SYT1* and *GRIK1*), both involved in synaptic function, TH and TAC3 populations present a negative pattern. The absence of *SYT1* and *GRIK1* expression is a distinctive feature that distinguishes both TAC3 in human and Th in mouse from all the other interneuron populations in their respective species. Although integration of human and mouse datasets was not technically possible, even despite applying recent tools such as LIGER⁵⁴, the aforementioned genes showed strong parallelism between the mouse Th and the human TAC3 populations. Importantly, in agreement with others²⁷, we hardly found any *TH*-expressing interneurons, although we did find *TH* expression in MSNs as shown elsewhere^{32,55,56}. This observation points out that *TH* expression in striatum probably cannot be used as a marker for this cell class, at least in humans, and suggests that, from the evolutionary perspective, the absence of *TH* in the TAC3 population might just indicate a refinement in the circuitry or a loss of unnecessary machinery. Noteworthy, since *TH* is the limiting enzyme in the synthesis of dopamine and noradrenaline, we also examined our data for genes related to dopamine metabolism and found none (data not shown).

Inner gradient structure is conserved in the human striatum

Because the discrete partitions of the data might not reveal the entire biologically relevant diversity of the striatal interneuron populations⁴⁹, we examined the PTHLH and TAC3 subclasses using factor analysis. With this approach, we did find that there is diversity within the subclasses, as indicated by differences in expression patterns along a continuum rather than by discrete changes in the expression of a set of marker genes. The gradients within each subtype were driven by the same set of genes in both the CN and the Pu. We also studied the gradient structure in the human striatum as previously shown in the

mouse striatum for both interneuron and MSNs^{20–22}. We found an inner gradient structure for the most abundant classes, TAC3 and PTHLH, which is shared in both CN and Pu, indicating similarities in structure, as it was shown for Pthlh in the mouse striatum²⁰. This gradient structure seems to be characteristic of subcortical structures such as the striatum and may reflect the need for a highly specialized organization to receive input from many different and distant brain areas.

Differences across regions

The main differences identified between CN and Pu in our study are related to the PTHLH class. Our results indicate that this cell class in the Pu might be involved in long-term potentiation mechanisms, a form of synaptic plasticity that plays a critical role in the proper functionality of the striatum^{9,57}. This difference may underscore a potentially different vulnerability of Pu vs CN to basal ganglia-related diseases, as already suggested by others^{58–60}, which could be used in the design of cell type-targeted therapeutic approaches.

Robustness of striatal interneuron taxonomy.

Besides performing *in situ* tissue validations of the interneuron classes and subclasses, we validated our taxonomy by integrating our data with previously published sn/cRNA-seq datasets. An unbiased clustering of the integrated data resulted in groups of interneurons that readily overlapped or at least related to each of the subclasses we describe here. More relevant, the expression profile of marker genes within each group was consistent across datasets, even in the non-integrated raw data. Our results indicate that our taxonomy is robust, as even the rarest cell subclasses could be observed in other datasets. Most notably, the classification we introduce was highly compatible with the samples from the nucleus accumbens (ventral striatum) from Tran et al²⁸, suggesting that the inhibitory neurons in both ventral and dorsal striatum share a similar diversity spectrum. However, a broader sampling of ventral striatum would be useful to reinforce this observation and to determine if this classification can be extended to other regions in the basal ganglia.

Material and Methods

Raw data and code

Single-cell RNA-seq data have been deposited at Figshare and are publicly available as of the date of publication (doi:10.6084/m9.figshare.22340140).

Data analysis code has been deposited at Figshare and is publicly available as of the date of publication. (doi:10.6084/m9.figshare.22340212).

Any additional information required to reanalyze the data reported in this paper is available from the lead contact upon request (Ana B. Muñoz-Manchado (ana.munoz@uca.es) .

Human tissue

Post-mortem human Pu (N = 28) and CN (N = 25) fresh frozen tissue samples from 28 donors without neurodegenerative features, age 25 to over 90 years were obtained from three sources, the Human Brain and Spinal Fluid Resource Center (Los Angeles, USA), the Parkinson's UK Brain Bank at Imperial (London, UK) and the Massachusetts Alzheimer's Disease Research Center (Charlestown, USA). Sample information can be found in Supplementary table 1. Given sex imbalance in our sample donors (9 females and 19 males), our study is underpowered to assess effects or influences due to sex, such as cell class proportion or regulation/effect on gene expression.

snRNA-seq data generation

Tissue dissociation

Isolation of nuclei from fresh frozen tissue was performed as described by the Allen Institute for Brain Science (<https://www.protocols.io/view/isolation-of-nuclei-from-adult-human-brain-tissue-eq2lyd1nqlx9/v2>) with the following specifications, all steps were performed at 4°C. 100–150 mg of tissue was thawed on ice and homogenized in 2 ml of chilled, nuclease-free homogenization buffer (10 mM Tris (pH 8), 250 mM Sucrose, 25 mM KCl, 5 mM MgCl₂, 0.1 mM DTT, 1x Protease inhibitor cocktail (50x in 100% Ethanol, G6521, Promega), 0.2 U/μl RNasin Plus (N2615, Promega), 0.1% Triton X-100) using a dounce tissue grinder with loose and tight pestle (20 strokes each, 357538, Wheaton). The nuclei solution was filtered through 70 μm and 30 μm strainers successively, tubes and strainers were washed with an additional homogenization buffer (final volume 6 ml) before centrifugation for 10 min at 900 rcf. Supernatant was removed leaving 50 μl above the pellet and resuspended in 200 μl homogenisation buffer (final volume 250 μl). Then, the suspension was carefully mixed 1:1 with 50% Iodixanol (OptiPrep Density Gradient Medium (D1556, Sigma) in 60 mM Tris (pH 8), 250 mM Sucrose, 150 mM KCl, 30 mM MgCl₂) and layered carefully on top of 500 μl 29% Iodixanol in a 1.5 ml tube. Samples were spun 20 min at 13500 rcf and supernatant was removed as much as possible without disrupting the pellet. Pellet was resuspended in 50 μl chilled, nuclease-free blocking buffer (1x PBS, 1% BSA, 0.2 U/μl RNasin Plus), transferred to a fresh tube and filled up to 500 μl. To enable enrichment of neurons during fluorescent activated cell sorting, 1 μl NeuN antibody (1:500, Millimark mouse anti-NeuN PE conjugated, FCMAB317PE, Merck) was added and samples were incubated for 30 min on ice in the dark. After spinning 5 min at 400 rcf, the supernatant was removed leaving ~ 50 μl of buffer above the pellets and 500 μl of blocking buffer was added to resuspend before filtering through a 20 μm filter into FACS tubes and adding 1 μl of DAPI (0.1 mg/ml, D3571, Invitrogen).

Fluorescent-activated nuclei sorting

Nuclei suspension was protected from light and sorted in a flow cytometer (DB FACSAria Fusion or BD FACSAria III) at 4°C. Gating was performed based on DAPI and phycoerythrin signal into two tubes containing 50 μl blocking buffer (NeuN + and NeuN- population) until 200000 nuclei per population were

reached. Sorted populations were centrifuged 4 min at 400 rcf and supernatant was removed, leaving approximately 30 µl to resuspend the pellet, samples were kept on ice.

library preparation

Library preparation from sorted nuclei suspension was done using the Chromium Next GEM Single Cell 3' Reagent Kit v3.1 (PN-1000268, 10x Genomics). Each nuclei population was counted manually, and the concentration was adjusted to a range between 200 and 1700 nuclei/µl. Following the manufacturer's protocol (CG000204 Rev D, 10x Genomics), RT mix was added to the nuclei suspension and samples were either loaded for each population on separate lanes (target nucleus recovery 5000) or population were mixed (70% NeuN+ and 30% NeuN, target nucleus recovery 5000 or 7000) before loading on one lane of the Chromium Next GEM Chip G (PN-1000120, 10x Genomics). Downstream cDNA synthesis and library preparation followed the manufacturer's instructions using the Single Index Kit T Set A (PN-1000213, 10x Genomics). Required quality control steps and quantification measurements within this protocol were performed using the Agilent High Sensitivity DNA Kit (5067 – 4626, Agilent Technologies) and the KAPA Library Quantification Kit (2700098952, Roche).

Illumina sequencing

Pools were prepared by combining up to 19 (target nucleus recovery 5000) or 16 (target nucleus recovery 7000) samples and sequencing was performed on a NovaSeq S6000 using a S4-200 (v1.5) flowcell with 8 lanes and a 28-8-0-91 read set up. The sequencing was performed at the National Genomics Infrastructure (Stockholm, Sweden).

High sensitivity in situ hybridization (FISH)

Tissue preparation for histology

Human tissue blocks (N = 6) were stored at -80°C and transferred to the cryostat (CryoStar NX70, Thermo Scientific) on dry ice. Samples were mounted on the specimen holder using Tissue Tek O.C.T. Compound (4583, Sakura) and acclimated to -20°C in the cryostat chamber for 5 minutes. 10 µm sections were cut and captured on Super-Frost Plus microscope slides (631 – 0108, VWR) at room temperature. Slides were air dried at room temperature for a few minutes and stored for 1h at -20°C before transferring them back to -80°C for long term storage.

RNAscope high sensitivity in-situ hybridization

High sensitivity in situ hybridization using the RNAscope Multiplex Fluorescent Reagent Kit v2 (323110, Advanced Cell Diagnostics) was performed on putamen sections of six subjects to detect single mRNA molecules. Experiments were performed according to the RNAscope Multiplex Fluorescent Reagent Kit v2 protocol (UM 323100, Advanced Cell Diagnostics) for the following genes: DACH1 (412041), NPY (416671-C2), PTHLH (452931), PVALB (422181-C2), SST (310591-C3). In brief, slides were dried at room temperature (RT) for 5–10 min before incubation in 4% PFA for 25 min at 4°C. Slides were washed twice in 1x PBS and dehydrated in 50%, 70% and 2x 100% ethanol for 5 min each at RT. After drying the slides

for 5 min, a hydrophobic barrier was drawn around each section prior to incubation in hydrogen peroxide for 10 min at RT. For antigen accessibility, slides were treated with Protease IV for 20 min at RT after a brief wash in 1x PBS. Slides were washed twice for 3 min again, before probes were incubated. C2 and C3 probes were diluted in C1 probes at a 1:50 ratio and incubated on the slides for 2h at 40°C. Slides were then incubated with amplification mix 1–3 followed by a combination of HRP reagent, fluorescent dye and HRP blocker specific for each probe channel in accordance with the manufacturer's recommendations. Probes were detected with Opal 520 (FP1487001, Akoya Biosciences), Opal 570 (FP1488001, Akoya Biosciences) and Opal 650 (FP1496001, Akoya Biosciences). Next, slides were incubated with TrueBlack (23007, Biotium) after a wash in 70% ethanol for 30 sec at RT to quench the autofluorescence due to the accumulation of lipofuscin or other protein aggregates. Prior to mounting with Fluoromount-G (0100-01, SouthernBiotech) the slices, DAPI was added to label the nuclei. A one-day protocol has been used in all experiments to preserve the quality of the slices.

Image acquisition

Confocal imaging was performed on a Zeiss LSM800-Airy with Zen software (2.6). 2–3 non-overlapping areas with a size of 8 x 8 tiles were selected per tissue section and images were acquired using a 20x air/dry objective. Final images were stitched using the according feature of the Zen software.

QUANTIFICATION AND STATISTICAL ANALYSIS

Image analysis

Quantitative image analysis was performed using the QuPath software (version 0.3.2,⁶¹) with the following workflow: (1) Definition of region of interest (ROI) on each image across all visible nuclei (using DAPI stain) but excluding artifacts and high fluorescent vessels, based on size and intensity of the signal. (2) Cell and subcellular detection tools of QuPath were adjusted for each staining (supplementary table 7) and applied within each ROI. (3) An object classifier was trained for each marker and subject individually by manual labeling of positive cells. Cells were considered positive when either a clear fluorescent signal was visible throughout the approximated cell body (NPY, SST) or a distinct puncta signal was evident with no overlapping signal in other fluorescent channels (DACH1, PTHLH, PVALB). The purpose of using object classifiers instead of counting subcellular spots directly was to improve the distinction between truly positive cells and cells with autofluorescent signal due to lipofuscin. (4) All relevant object classifiers for a specific staining and subject were combined to a composite classifier and applied to all RIO of the respective subject. (5) The resulting list of cells and their assigned markers per RIO were exported and evaluated for each subject within a staining. Among the group of positive cells minimum cut off values concerning the number of subcellular spots were defined for each marker (supplementary table 7) and applied manually. Additionally unexpected marker combinations or numbers of spots were checked manually on the image and corrected if necessary.

scRNA-seq data analysis

Pre-processing

The raw scRNA-seq data was processed into count matrices by using CellRanger (v.3.0.0) (10X genomics) to align the sequencing data to the hg38 genome (GRCh38.p5 (NCBI:GCA_000001405.20), accounting for both intronic and exonic sequences.

Quality Control

To detect possible doublets, we applied scrublet⁶² to each individual sample 100 times with automated threshold value detection, default parameters and a random seed. Nuclei labeled as doublets on more than 10% of the scrublet runs were discarded. Based on the distribution of UMIs and unique genes detected per nucleus, cells with less than 500 UMIs or 1200 genes were discarded. Cells with more than 250000 UMIs, over 15000 genes or more than 10% mitochondrial content were also excluded. Using the nuclei which passed the initial QC thresholds, we modeled the relationship between number of unique genes and UMIs in the logarithmic scale as a second-degree polynomial function. Nuclei with extreme deviations from the polynomial fit (a difference over 2000 between $\log(n_genes)$ and the value predicted by the fit for a given UMI count) were considered outliers and excluded from the rest of the analysis. Cells expressing high levels of marker genes for multiple cell types simultaneously were also discarded. To do so, we computed a cell-type score for each cell subtype (Oligos, Microglia, OPCs, Neurons, Astrocytes, Vascular cells) for each nucleus. This score was the mean expression of the canonical markers for each type. Then we computed the distribution of the scores on the whole dataset, observing bimodal distributions in all cases. We modelled the distributions as mixtures of two gaussians and set a threshold on the mean of the lowest distribution plus four times its standard deviation. Nuclei with a score above the threshold were considered of a given cell type. Nuclei with scores above the threshold for more than one type were considered doublets and excluded from the rest of the analysis. To remove possible contamination from the claustrum or the amygdala, we removed cells expressing regional markers obtained from the Allen Brain atlas (ref): NEUROD2, TMEM155, CARTPT, SLC17A7. The number of nuclei excluded at each step of this process is detailed in Supplementary Fig. 1.

Interneuron detection

The count matrices were analyzed using Scanpy⁶³ to cluster and label them in order to select for interneurons. We performed principal component analysis and computed the neighborhood graph on the first 30 principal components (PCs). The data was then clustered using the louvain algorithm⁶⁴ with a resolution of 0.2 and the clusters were labeled as either glia or neurons based on the expression of canonical markers:

Astrocytes – *AQP4*, *ADGRV1*

Microglia – *CSF1R*, *FYB1*

Oligodendrocytes – *MBP*, *MOG*, *MAG*

Oligodendrocyte precursor cells – *PTPRZ1, PDGFRA, VCAN*

Vascular cells – *EBF1, ABCB1, ABCA9*

Neurons – *MEG3*

The neurons were filtered again based on their distribution of UMIs and genes. Nuclei labeled as neurons with less than 5000 UMIs, less than 3000 genes or more than 12000 genes were discarded, resulting in a total of 181434 high quality neuronal nuclei. The neurons were re-clustered after removing sex-linked mitochondrial and riboprotein genes, projecting them onto their first 30 PCs computed on their 1500 most variable genes. The clusters expressing the inhibitory markers *GAD1* and/or *GAD2* and not expressing *MSN* (*PPP1R1B, DRD1, DRD2, MEIS2*) or excitatory markers (*RORB*) were labeled as interneurons.

Interneuron classification

Nuclei labeled as interneurons were projected onto the first 20 PCs calculated on their 1500 most variable genes and re-clustered using the louvain algorithm. The function `rank_genes_groups` from `scanpy`⁶³ was used to perform a differential expression analysis between the clusters through a Wilcoxon rank-sum test. Marker genes were selected manually from the top ranked genes to characterize and name each of the interneuron clusters as a different interneuron subclass. The interneuron subtypes were merged into broader classes based on their correlation. All subtypes with a mean Pearson correlation coefficient higher than 0.49 to each other were joined into a broader class defined by common marker genes. The dendrograms were computed using the average Pearson correlation coefficient between groups across all genes.

Compositional analysis

The differences in composition between the CN and the Pu were examined through the centered-log ratio (CLR)⁶⁵ values for each interneuron class on each of the regions. This measure is defined as

$$CLR_x = \log \left(\frac{r_x}{g} \right)$$

Where r_x is the fraction of interneurons of a given class and g is the geometric mean of the fractions of each of the classes. The distribution of CLR values for the same interneuron class were compared across regions using a non-parametric Wilcoxon test.

Differential expression analysis (DEA)

Regional changes in gene expression were studied using a pseudo-bulk approach in which the nuclei were aggregated by region and sample. The `Libra` python library⁶⁶ was used to perform the data aggregation and the differential expression analysis, which was done using the `edgeR-LRT` method⁶⁷. In all the other cases, differential gene expression was studied at the cell level using the `rank_genes_groups` function from the `scanpy` library using a Wilcoxon rank-sum test.

Over-Representation Analysis (ORA)

Differentially Expressed Genes (DEGs) derived from DEA were used as input into the enrichGO and enrichKEGG functions from the R package clusterProfiler⁶⁸. DEGs with a logFC > 0.5 and p-adjusted value < 0.05 were selected. The first function generates functional Gene Ontology terms⁶⁹ related to biological processes, molecular function, and cellular components. The second function analyzes the enriched terms in our gene list based on the KEGG database⁷⁰. This database is a collection of manually drawn pathway maps representing our knowledge of the molecular interaction, reaction, and relation networks for Metabolism, Genetic Information Processing, Environmental Information Processing, Cellular Processes, Organismal Systems, Human Diseases, and Drug Development. Terms with a p-value < 0.1 were selected and plotted using the GOplot package⁷¹.

Factor analysis

The heterogeneity within the PTHLH and TAC3 subclasses was studied using a factor analysis. For each interneuron subclass on each of the two striatal regions, we removed the sex-linked, mitochondrial and riboprotein genes, and then restricted the data to the 1200 most variable genes. We then applied the FactorAnalysis function from the scikit-learn Python library⁷² with a single latent factor to perform a matrix decomposition.

Data projection on functional gene subsets

To restrict the data to neurotransmitter-receptor genes, we selected genes based on their prefixes: DRD- (dopamine); GABR- (GABA); CHRN-, CHRM- (acetylcholine); GRIA-, GRIN-, GRIK-, GRM-, GRID-, GRIP- (glutamine). We added three additional glutamine receptors whose naming did not follow the same pattern: *PEPL1*, *POLR2M*, *GCOM1*. This selection resulted in 93 genes. To study the genes with ion channel receptors, we restricted our data to the genes listed under the GO-term GO:0005216. This list contained 481 genes names, out of which 431 were found in our data. In both cases, we obtained the UMAP projection from the neighborhood graph computed on the first 30 PCs and then performed a differential expression analysis across interneuron subclasses using a Wilcoxon rank-sum test.

Public datasets collection and pre-processing

We collected two single-nuclei RNA-seq datasets of the human striatum from the GEO database⁷³, with accession numbers GSE151761²⁷ and GSE152058²⁹. A third dataset²⁷ was obtained from a public repository setup by the authors (https://github.com/LieberInstitute/10xPilot_snRNAseq-human)²⁸. On Krienen *et al.*'s data, we analyzed separately the 10X and Drop-Seq datasets. On Lee *et al.*'s data we used only the nuclei belonging to control subjects (8 samples). We normalized all the datasets using scran normalization⁷⁴ and applied individual QC filters to remove bad quality nuclei. We then clustered the data and selected the interneuronal populations using the same approach and criteria that we applied to our own data. Notably, on Lee *et al.*'s dataset our selection included a cluster originally labeled as secretory

ependymal cells, which expressed both pan-neuronal and interneuronal markers, and we identified as TAC3 interneurons. The total number of cells filtered and selected are detailed in Supplementary table 6.

The mouse data from Muñoz-Manchado et al.²⁰ was obtained from the GEO database (accession number GSE97478). The raw counts were normalized using the *normalize_total* function from scanpy, with a target sum of 10000 per cell. The original labels were retained, and the data was not transformed further.

Data integration

snRNA-seq dataset from multiple sources were integrated using scVI³⁶. First, the data was merged and restricted to the 12986 genes common across datasets. Then the 1200 most variable genes were selected and used to build and train an autoencoder with 1 hidden layer of 128 nodes and a latent space of dimensionality 12 which was trained for 292 epochs. The low-dimensional latent state representation was used to build a neighborhood graph and then cluster the data in the same way as on the PC-projected data from our novel dataset.

Declarations

Acknowledgments

The authors acknowledge the Massachusetts Alzheimer's Disease Research Center (especially Patrick Dooley and Tessa Connors), the Parkinson's UK Brain Bank at Imperial funded by Parkinson's UK (a charity registered in England and Wales, 258197, and in Scotland, SC037554), and the NIH NeuroBioBank (NIH Ref-1851, Requestor: Ernest Arenas), for the supply of tissue samples and associated clinical and neuropathological data. The authors acknowledge support to A.B.M.-M from the Spanish Ministry of Science and Innovation (I+D+i, PID2019-109046GA-I00, RyC programme), the Swedish Foundation for Strategic Research (FFL 18-0314), and the Swedish Research Council (2017-03349), and to B.T.H and A.S.-P from the US National Institute on Aging (P30 AG062421 and K08AG064039 respectively). The authors also want to thank the National Genomics Infrastructure in Stockholm funded by Science for Life Laboratory and SNIC/Uppsala Multidisciplinary Center for Advanced Computational Science for assistance with massively parallel sequencing and access to the UPPMAX computational infrastructure. We also thank the donors and their families who have contributed to this study.

Author contributions

L.G., L.H. and A.B.M.-M designed the study. L.H., M.D.-S and A.B.M.-M carried out experiments, L.G., J.M.B.-R, L.H. and A.B.M.-M performed data analysis; A.S.-P, B.T.H provided resources, A.B.M.-M secured funding; L.G., L.H. and A.B.M.-M wrote the manuscript with comments and reviewing from all authors.

Competing interests.

The authors declare no competing interests.

References

1. Fix, J.D. (2008). *Neuroanatomy: includes online access to full text and questions from the book!* 4th ed. (Wolters Kluwer, Lippincott Williams & Wilkins).
2. Przedborski, S. (2017). The two-century journey of Parkinson disease research. *Nat Rev Neurosci* *18*, 251–259. 10.1038/nrn.2017.25.
3. Shen, W., Zhai, S., and Surmeier, D.J. (2022). Striatal synaptic adaptations in Parkinson's disease. *Neurobiology of Disease* *167*, 105686. 10.1016/j.nbd.2022.105686.
4. Pini, L., Pievani, M., Bocchetta, M., Altomare, D., Bosco, P., Cavedo, E., Galluzzi, S., Marizzoni, M., and Frisoni, G.B. (2016). Brain atrophy in Alzheimer's Disease and aging. *Ageing Research Reviews* *30*, 25–48. 10.1016/j.arr.2016.01.002.
5. Matsushima, A., Pineda, S.S., Crittenden, J.R., Lee, H., Galani, K., Mantero, J., Tombaugh, G., Kellis, M., Heiman, M., and Graybiel, A.M. (2023). Transcriptional vulnerabilities of striatal neurons in human and rodent models of Huntington's disease. *Nat Commun* *14*, 282. 10.1038/s41467-022-35752-x.
6. Robbins, T.W., Vaghi, M.M., and Banca, P. (2019). Obsessive-Compulsive Disorder: Puzzles and Prospects. *Neuron* *102*, 27–47. 10.1016/j.neuron.2019.01.046.
7. Simpson, E.H., Kellendonk, C., and Kandel, E. (2010). A Possible Role for the Striatum in the Pathogenesis of the Cognitive Symptoms of Schizophrenia. *Neuron* *65*, 585–596. 10.1016/j.neuron.2010.02.014.
8. Major Depressive Disorder Working Group of the Psychiatric Genomics Consortium, Skene, N.G., Bryois, J., Bakken, T.E., Breen, G., Crowley, J.J., Gaspar, H.A., Giusti-Rodriguez, P., Hodge, R.D., Miller, J.A., et al. (2018). Genetic identification of brain cell types underlying schizophrenia. *Nat Genet* *50*, 825–833. 10.1038/s41588-018-0129-5.
9. Kreitzer, A.C., and Malenka, R.C. (2008). Striatal Plasticity and Basal Ganglia Circuit Function. *Neuron* *60*, 543–554. 10.1016/j.neuron.2008.11.005.
10. DiFiglia, M., Pasik, P., and Pasik, T. (1976). A Golgi study of neuronal types in the neostriatum of monkeys. *Brain Research* *114*, 245–256. 10.1016/0006-8993(76)90669-7.
11. Cavaccini, A., Gritti, M., Giorgi, A., Locarno, A., Heck, N., Migliarini, S., Bertero, A., Mereu, M., Margiani, G., Trusel, M., et al. (2018). Serotonergic Signaling Controls Input-Specific Synaptic Plasticity at Striatal Circuits. *Neuron* *98*, 801-816.e7. 10.1016/j.neuron.2018.04.008.
12. Lerner, T.N., Shilyansky, C., Davidson, T.J., Evans, K.E., Beier, K.T., Zalocusky, K.A., Crow, A.K., Malenka, R.C., Luo, L., Tomer, R., et al. (2015). Intact-Brain Analyses Reveal Distinct Information Carried by SNc Dopamine Subcircuits. *Cell* *162*, 635–647. 10.1016/j.cell.2015.07.014.
13. Graveland, G.A., Williams, R.S., and DiFiglia, M. (1985). A Golgi study of the human neostriatum: Neurons and afferent fibers. *J. Comp. Neurol.* *234*, 317–333. 10.1002/cne.902340304.
14. Tepper, J.M., Koós, T., Ibanez-Sandoval, O., Tecuapetla, F., Faust, T.W., and Assous, M. (2018). Heterogeneity and Diversity of Striatal GABAergic Interneurons: Update 2018. *Front. Neuroanat.* *12*, 91. 10.3389/fnana.2018.00091.

15. Muñoz-Manchado, A.B., Foldi, C., Szydlowski, S., Sjulson, L., Farries, M., Wilson, C., Silberberg, G., and Hjerling-Leffler, J. (2016). Novel Striatal GABAergic Interneuron Populations Labeled in the 5HT3a^{EGFP} Mouse. *Cereb. Cortex* *26*, 96–105. 10.1093/cercor/bhu179.
16. Rudy, B., Fishell, G., Lee, S., and Hjerling-Leffler, J. (2011). Three groups of interneurons account for nearly 100% of neocortical GABAergic neurons. *Devel Neurobio* *71*, 45–61. 10.1002/dneu.20853.
17. Zeisel, A., Hochgerner, H., Lönnerberg, P., Johnsson, A., Memic, F., van der Zwan, J., Häring, M., Braun, E., Borm, L.E., La Manno, G., et al. (2018). Molecular Architecture of the Mouse Nervous System. *Cell* *174*, 999-1014.e22. 10.1016/j.cell.2018.06.021.
18. Zeisel, A., Muñoz-Manchado, A.B., Codeluppi, S., Lönnerberg, P., La Manno, G., Juréus, A., Marques, S., Munguba, H., He, L., Betsholtz, C., et al. (2015). Cell types in the mouse cortex and hippocampus revealed by single-cell RNA-seq. *Science* *347*, 1138–1142. 10.1126/science.aaa1934.
19. Bakken, T.E., Jorstad, N.L., Hu, Q., Lake, B.B., Tian, W., Kalmbach, B.E., Crow, M., Hodge, R.D., Krienen, F.M., Sorensen, S.A., et al. (2021). Comparative cellular analysis of motor cortex in human, marmoset and mouse. *Nature* *598*, 111–119. 10.1038/s41586-021-03465-8.
20. Muñoz-Manchado, A.B., Bengtsson Gonzales, C., Zeisel, A., Munguba, H., Bekkouche, B., Skene, N.G., Lönnerberg, P., Ryge, J., Harris, K.D., Linnarsson, S., et al. (2018). Diversity of Interneurons in the Dorsal Striatum Revealed by Single-Cell RNA Sequencing and PatchSeq. *Cell Reports* *24*, 2179-2190.e7. 10.1016/j.celrep.2018.07.053.
21. Gokce, O., Stanley, G.M., Treutlein, B., Neff, N.F., Camp, J.G., Malenka, R.C., Rothwell, P.E., Fuccillo, M.V., Südhof, T.C., and Quake, S.R. (2016). Cellular Taxonomy of the Mouse Striatum as Revealed by Single-Cell RNA-Seq. *Cell Reports* *16*, 1126–1137. 10.1016/j.celrep.2016.06.059.
22. Stanley, G., Gokce, O., Malenka, R.C., Südhof, T.C., and Quake, S.R. (2020). Continuous and Discrete Neuron Types of the Adult Murine Striatum. *Neuron* *105*, 688-699.e8. 10.1016/j.neuron.2019.11.004.
23. Bengtsson Gonzales, C., Hunt, S., Munoz-Manchado, A.B., McBain, C.J., and Hjerling-Leffler, J. (2020). Intrinsic electrophysiological properties predict variability in morphology and connectivity among striatal Parvalbumin-expressing Pthlh-cells. *Sci Rep* *10*, 15680. 10.1038/s41598-020-72588-1.
24. Lecumberri, A., Lopez-Janeiro, A., Corral-Domenge, C., and Bernacer, J. (2017). Neuronal density and proportion of interneurons in the associative, sensorimotor and limbic human striatum. *Brain Struct Funct*. 10.1007/s00429-017-1579-8.
25. Bernácer, J., Prensa, L., and Giménez-Amaya, J.M. (2007). Cholinergic Interneurons Are Differentially Distributed in the Human Striatum. *PLoS ONE* *2*, e1174. 10.1371/journal.pone.0001174.
26. del Rey, N.L., Trigo-Damas, I., Obeso, J.A., Cavada, C., and Blesa, J. (2022). Neuron types in the primate striatum: Stereological analysis of projection neurons and interneurons in control and parkinsonian monkeys. *Neuropathology Appl Neurobio* *48*. 10.1111/nan.12812.
27. Krienen, F.M., Goldman, M., Zhang, Q., C. H. del Rosario, R., Florio, M., Machold, R., Saunders, A., Levandowski, K., Zaniewski, H., Schuman, B., et al. (2020). Innovations present in the primate interneuron repertoire. *Nature* *586*, 262–269. 10.1038/s41586-020-2781-z.

28. Tran, M.N., Maynard, K.R., Spangler, A., Huuki, L.A., Montgomery, K.D., Sadashivaiah, V., Tippani, M., Barry, B.K., Hancock, D.B., Hicks, S.C., et al. (2021). Single-nucleus transcriptome analysis reveals cell-type-specific molecular signatures across reward circuitry in the human brain. *Neuron* *109*, 3088-3103.e5. 10.1016/j.neuron.2021.09.001.
29. Lee, H., Fenster, R.J., Pineda, S.S., Gibbs, W.S., Mohammadi, S., Davila-Velderrain, J., Garcia, F.J., Therrien, M., Novis, H.S., Gao, F., et al. (2020). Cell Type-Specific Transcriptomics Reveals that Mutant Huntingtin Leads to Mitochondrial RNA Release and Neuronal Innate Immune Activation. *Neuron* *107*, 891-908.e8. 10.1016/j.neuron.2020.06.021.
30. Neves, S.R., Ram, P.T., and Iyengar, R. (2002). G Protein Pathways. *Science* *296*, 1636–1639. 10.1126/science.1071550.
31. Ni, R.-J., Shu, Y.-M., Li, T., and Zhou, J.-N. (2021). Whole-Brain Afferent Inputs to the Caudate Nucleus, Putamen, and Accumbens Nucleus in the Tree Shrew Striatum. *Front. Neuroanat.* *15*, 763298. 10.3389/fnana.2021.763298.
32. Saunders, A., Macosko, E.Z., Wysoker, A., Goldman, M., Krienen, F.M., de Rivera, H., Bien, E., Baum, M., Bortolin, L., Wang, S., et al. (2018). Molecular Diversity and Specializations among the Cells of the Adult Mouse Brain. *Cell* *174*, 1015-1030.e16. 10.1016/j.cell.2018.07.028.
33. Erisir, A., Lau, D., Rudy, B., and Leonard, C.S. (1999). Function of Specific K⁺ Channels in Sustained High-Frequency Firing of Fast-Spiking Neocortical Interneurons. *Journal of Neurophysiology* *82*, 2476–2489. 10.1152/jn.1999.82.5.2476.
34. Okaty, B.W., Miller, M.N., Sugino, K., Hempel, C.M., and Nelson, S.B. (2009). Transcriptional and Electrophysiological Maturation of Neocortical Fast-Spiking GABAergic Interneurons. *J. Neurosci.* *29*, 7040–7052. 10.1523/JNEUROSCI.0105-09.2009.
35. Gu, Y., Servello, D., Han, Z., Lalchandani, R.R., Ding, J.B., Huang, K., and Gu, C. (2018). Balanced Activity between Kv3 and Nav Channels Determines Fast-Spiking in Mammalian Central Neurons. *iScience* *9*, 120–137. 10.1016/j.isci.2018.10.014.
36. Lopez, R., Regier, J., Cole, M.B., Jordan, M.I., and Yosef, N. (2018). Deep generative modeling for single-cell transcriptomics. *Nat Methods* *15*, 1053–1058. 10.1038/s41592-018-0229-2.
37. Huang, Z.J., and Paul, A. (2019). The diversity of GABAergic neurons and neural communication elements. *Nat Rev Neurosci* *20*, 563–572. 10.1038/s41583-019-0195-4.
38. Ernst, A., Alkass, K., Bernard, S., Salehpour, M., Perl, S., Tisdale, J., Possnert, G., Druid, H., and Frisén, J. (2014). Neurogenesis in the Striatum of the Adult Human Brain. *Cell* *156*, 1072–1083. 10.1016/j.cell.2014.01.044.
39. Araújo de Góis Morais, P.L., de Souza Cavalcante, J., Engelberth, R.C., Guzen, F.P., Junior, E.S.N., and Paiva Cavalcanti, J.R.L. (2023). Morphology and morphometry of interneuron subpopulations of the marmoset monkey (*Callithrix jacchus*) striatum. *Neuroscience Research*, S0168010223000366. 10.1016/j.neures.2023.02.002.
40. Tepper, J.M., Tecuapetla, F., Koós, T., and Ibáñez-Sandoval, O. (2010). Heterogeneity and Diversity of Striatal GABAergic Interneurons. *Front. Neuroanat.* *4*. 10.3389/fnana.2010.00150.

41. Tasic, B., Yao, Z., Graybuck, L.T., Smith, K.A., Nguyen, T.N., Bertagnolli, D., Goldy, J., Garren, E., Economo, M.N., Viswanathan, S., et al. (2018). Shared and distinct transcriptomic cell types across neocortical areas. *Nature* *563*, 72–78. 10.1038/s41586-018-0654-5.
42. Knowles, R., Dehorter, N., and Ellender, T. (2021). From Progenitors to Progeny: Shaping Striatal Circuit Development and Function. *J. Neurosci.* *41*, 9483–9502. 10.1523/JNEUROSCI.0620-21.2021.
43. Ma, T., Zhang, Q., Cai, Y., You, Y., Rubenstein, J.L.R., and Yang, Z. (2012). A Subpopulation of Dorsal Lateral/Caudal Ganglionic Eminence-Derived Neocortical Interneurons Expresses the Transcription Factor Sp8. *Cerebral Cortex* *22*, 2120–2130. 10.1093/cercor/bhr296.
44. Ma, Y., and Giardino, W.J. (2022). Neural circuit mechanisms of the cholecystinin (CCK) neuropeptide system in addiction. *Addiction Neuroscience* *3*, 100024. 10.1016/j.addicn.2022.100024.
45. Castiglioni, V., Faedo, A., Onorati, M., Bocchi, V.D., Li, Z., Iennaco, R., Vuono, R., Bulfamante, G.P., Muzio, L., Martino, G., et al. (2019). Dynamic and Cell-Specific DACH1 Expression in Human Neocortical and Striatal Development. *Cerebral Cortex* *29*, 2115–2124. 10.1093/cercor/bhy092.
46. Nosaka, D., and Wickens, J.R. (2022). Striatal Cholinergic Signaling in Time and Space. *Molecules* *27*, 1202. 10.3390/molecules27041202.
47. Kocaturk, S., Guven, E.B., Shah, F., Tepper, J.M., and Assous, M. (2022). Cholinergic control of striatal GABAergic microcircuits. *Cell Reports* *41*, 111531. 10.1016/j.celrep.2022.111531.
48. Trapnell, C. (2015). Defining cell types and states with single-cell genomics. *Genome Res.* *25*, 1491–1498. 10.1101/gr.190595.115.
49. Kiselev, V.Y., Andrews, T.S., and Hemberg, M. (2019). Challenges in unsupervised clustering of single-cell RNA-seq data. *Nat Rev Genet* *20*, 273–282. 10.1038/s41576-018-0088-9.
50. Wagner, A., Regev, A., and Yosef, N. (2016). Revealing the vectors of cellular identity with single-cell genomics. *Nat Biotechnol* *34*, 1145–1160. 10.1038/nbt.3711.
51. Zeng, H., and Sanes, J.R. (2017). Neuronal cell-type classification: challenges, opportunities and the path forward. *Nat Rev Neurosci* *18*, 530–546. 10.1038/nrn.2017.85.
52. Ibanez-Sandoval, O., Tecuapetla, F., Unal, B., Shah, F., Koos, T., and Tepper, J.M. (2010). Electrophysiological and Morphological Characteristics and Synaptic Connectivity of Tyrosine Hydroxylase-Expressing Neurons in Adult Mouse Striatum. *Journal of Neuroscience* *30*, 6999–7016. 10.1523/JNEUROSCI.5996-09.2010.
53. Luo, R., Janssen, M.J., Partridge, J.G., and Vicini, S. (2013). Direct and GABA-mediated indirect effects of nicotinic ACh receptor agonists on striatal neurones: Nicotinic receptors in striatal interneurons. *The Journal of Physiology* *591*, 203–217. 10.1113/jphysiol.2012.241786.
54. Liu, J., Gao, C., Sodicoff, J., Kozareva, V., Macosko, E.Z., and Welch, J.D. (2020). Jointly defining cell types from multiple single-cell datasets using LIGER. *Nat Protoc* *15*, 3632–3662. 10.1038/s41596-020-0391-8.
55. Mao, M., Nair, A., and Augustine, G.J. (2019). A Novel Type of Neuron Within the Dorsal Striatum. *Front. Neural Circuits* *13*, 32. 10.3389/fncir.2019.00032.

56. Darmopil, S., Muñetón-Gómez, V.C., de Ceballos, M.L., Bernson, M., and Moratalla, R. (2008). Tyrosine hydroxylase cells appearing in the mouse striatum after dopamine denervation are likely to be projection neurones regulated by l-DOPA. *Eur J Neurosci* 27, 580–592. 10.1111/j.1460-9568.2008.06040.x.
57. Mancini, A., de Iure, A., and Picconi, B. (2022). Basic mechanisms of plasticity and learning. In *Handbook of Clinical Neurology* (Elsevier), pp. 21–34. 10.1016/B978-0-12-819410-2.00002-3.
58. Owens-Walton, C., Jakabek, D., Power, B.D., Walterfang, M., Hall, S., van Westen, D., Looi, J.C.L., Shaw, M., and Hansson, O. (2021). Structural and functional neuroimaging changes associated with cognitive impairment and dementia in Parkinson's disease. *Psychiatry Research: Neuroimaging* 312, 111273. 10.1016/j.psychres.2021.111273.
59. Brooks, D.J., Ibanez, V., Sawle, G.V., Quinn, N., Lees, A.J., Mathias, C.J., Bannister, R., Marsden, C.D., and Frackowiak, R.S.J. (1990). Differing patterns of striatal 18F-dopa uptake in Parkinson's disease, multiple system atrophy, and progressive supranuclear palsy. *Ann Neurol*. 28, 547–555. 10.1002/ana.410280412.
60. Kish, S.J., Shannak, K., and Hornykiewicz, O. (1988). Uneven Pattern of Dopamine Loss in the Striatum of Patients with Idiopathic Parkinson's Disease. *N Engl J Med* 318, 876–880. 10.1056/NEJM198804073181402.
61. Bankhead, P., Loughrey, M.B., Fernández, J.A., Dombrowski, Y., McArt, D.G., Dunne, P.D., McQuaid, S., Gray, R.T., Murray, L.J., Coleman, H.G., et al. (2017). QuPath: Open source software for digital pathology image analysis. *Sci Rep* 7, 16878. 10.1038/s41598-017-17204-5.
62. Wolock, S.L., Lopez, R., and Klein, A.M. (2019). Scrublet: Computational Identification of Cell Doublets in Single-Cell Transcriptomic Data. *Cell Systems* 8, 281-291.e9. 10.1016/j.cels.2018.11.005.
63. Wolf, F.A., Angerer, P., and Theis, F.J. (2018). SCANPY: large-scale single-cell gene expression data analysis. *Genome Biol* 19, 15. 10.1186/s13059-017-1382-0.
64. Traag, V.A., Waltman, L., and van Eck, N.J. (2019). From Louvain to Leiden: guaranteeing well-connected communities. *Sci Rep* 9, 5233. 10.1038/s41598-019-41695-z.
65. Quinn, T.P., Erb, I., Richardson, M.F., and Crowley, T.M. (2018). Understanding sequencing data as compositions: an outlook and review. *Bioinformatics* 34, 2870–2878.
66. Squair, J.W., Gautier, M., Kathe, C., Anderson, M.A., James, N.D., Hutson, T.H., Hudelle, R., Qaiser, T., Matson, K.J.E., Barraud, Q., et al. (2021). Confronting false discoveries in single-cell differential expression. *Nat Commun* 12, 5692. 10.1038/s41467-021-25960-2.
67. Robinson, M.D., McCarthy, D.J., and Smyth, G.K. (2010). edgeR: a Bioconductor package for differential expression analysis of digital gene expression data. *Bioinformatics* 26, 139–140. 10.1093/bioinformatics/btp616.
68. Wu, T., Hu, E., Xu, S., Chen, M., Guo, P., Dai, Z., Feng, T., Zhou, L., Tang, W., Zhan, L., et al. (2021). clusterProfiler 4.0: A universal enrichment tool for interpreting omics data. *The Innovation* 2, 100141. 10.1016/j.xinn.2021.100141.

69. Mi, H., Muruganujan, A., Ebert, D., Huang, X., and Thomas, P.D. (2019). PANTHER version 14: more genomes, a new PANTHER GO-slim and improvements in enrichment analysis tools. *Nucleic Acids Research* *47*, D419–D426. 10.1093/nar/gky1038.
70. Kanehisa, M. (2000). KEGG: Kyoto Encyclopedia of Genes and Genomes. *Nucleic Acids Research* *28*, 27–30. 10.1093/nar/28.1.27.
71. Walter, W., Sánchez-Cabo, F., and Ricote, M. (2015). GOplot: an R package for visually combining expression data with functional analysis. *Bioinformatics* *31*, 2912–2914. 10.1093/bioinformatics/btv300.
72. Pedregosa, F., Varoquaux, G., Gramfort, A., Michel, V., Thirion, B., Grisel, O., Blondel, M., Müller, A., Nothman, J., Louppe, G., et al. (2012). Scikit-learn: Machine Learning in Python. 10.48550/ARXIV.1201.0490.
73. Barrett, T., Suzek, T.O., Troup, D.B., Wilhite, S.E., Ngau, W.-C., Ledoux, P., Rudnev, D., Lash, A.E., Fujibuchi, W., and Edgar, R. (2005). NCBI GEO: mining millions of expression profiles—database and tools. *Nucleic Acids Research* *33*, D562–D566. 10.1093/nar/gki022.
74. Lun, A.T.L., McCarthy, D.J., and Marioni, J.C. (2016). A step-by-step workflow for low-level analysis of single-cell RNA-seq data with Bioconductor. 10.12688/f1000research.9501.2.

Figures

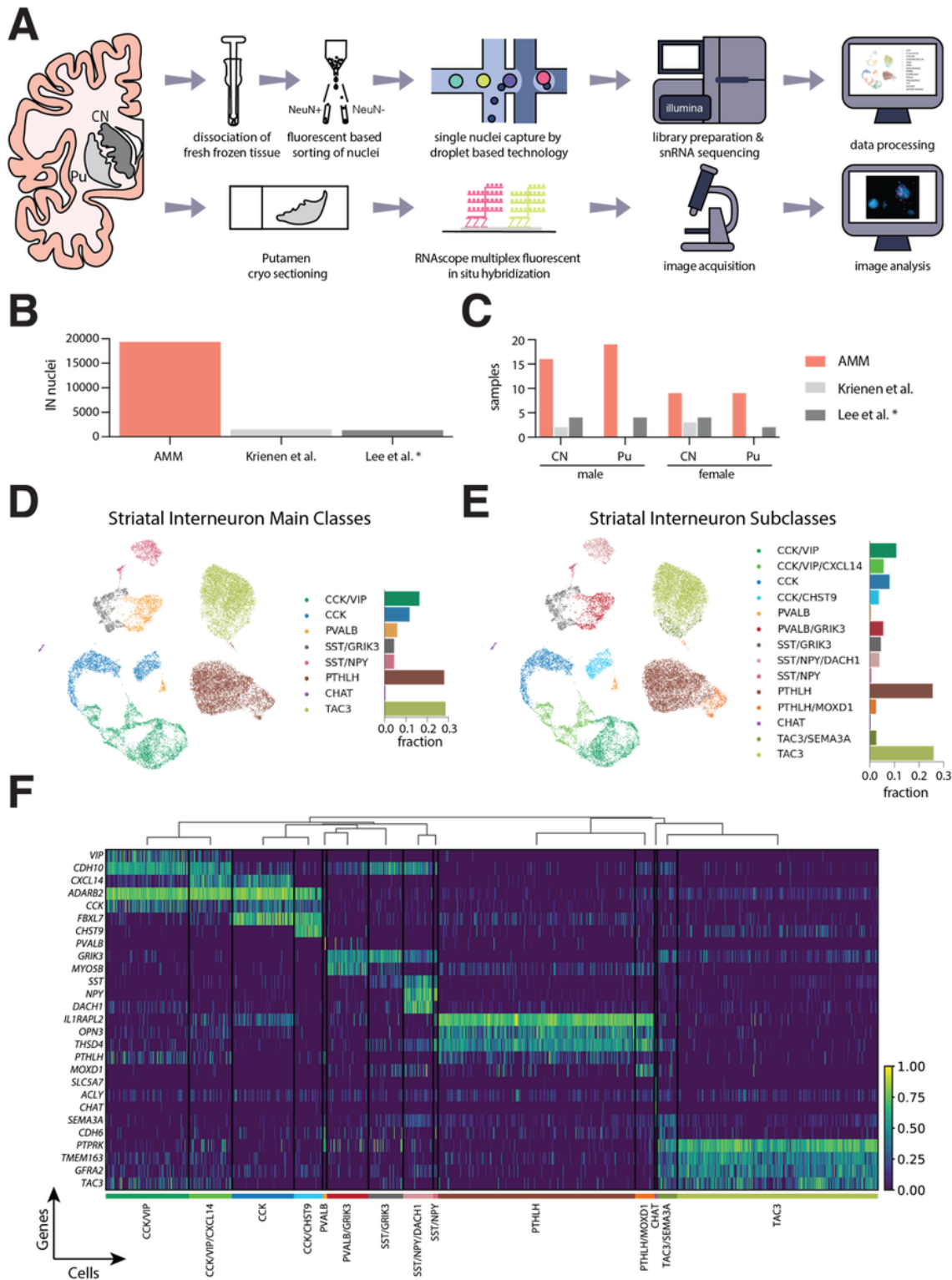


Figure 1

Interneuron heterogeneity of the human striatum determined by single-nucleus RNA-sequencing. A. Schematic overview of the experimental design. **B.** Number of interneuron nuclei sequenced in the present study (labeled as AMM) vs. two other previous works. **C.** Number of human samples included in this study (AMM) vs. two previous works. **D.** UMAP projection of the snRNA-seq data of the nuclei labeled as interneurons, colored by class. The barplot next to the UMAP indicates the fraction of all interneuron

nuclei represented by each class. **E.** UMAP projection of the interneuron nuclei colored by subclass. The barplot indicates the fraction of each subclass over all interneuron nuclei. **F.** Heatmap showing the expression of selected marker genes for each of the fourteen interneuron subclasses identified. The expression of each gene is normalized by its maximum value across all nuclei. The dendrogram above the heatmap indicates the proximity across subclasses based on the average Pearson correlation coefficient across all genes between each pair of subclasses. * Note that only the samples from control donors are shown in here from Lee's study. CN, caudate nucleus; IN, interneuron; Pu, putamen

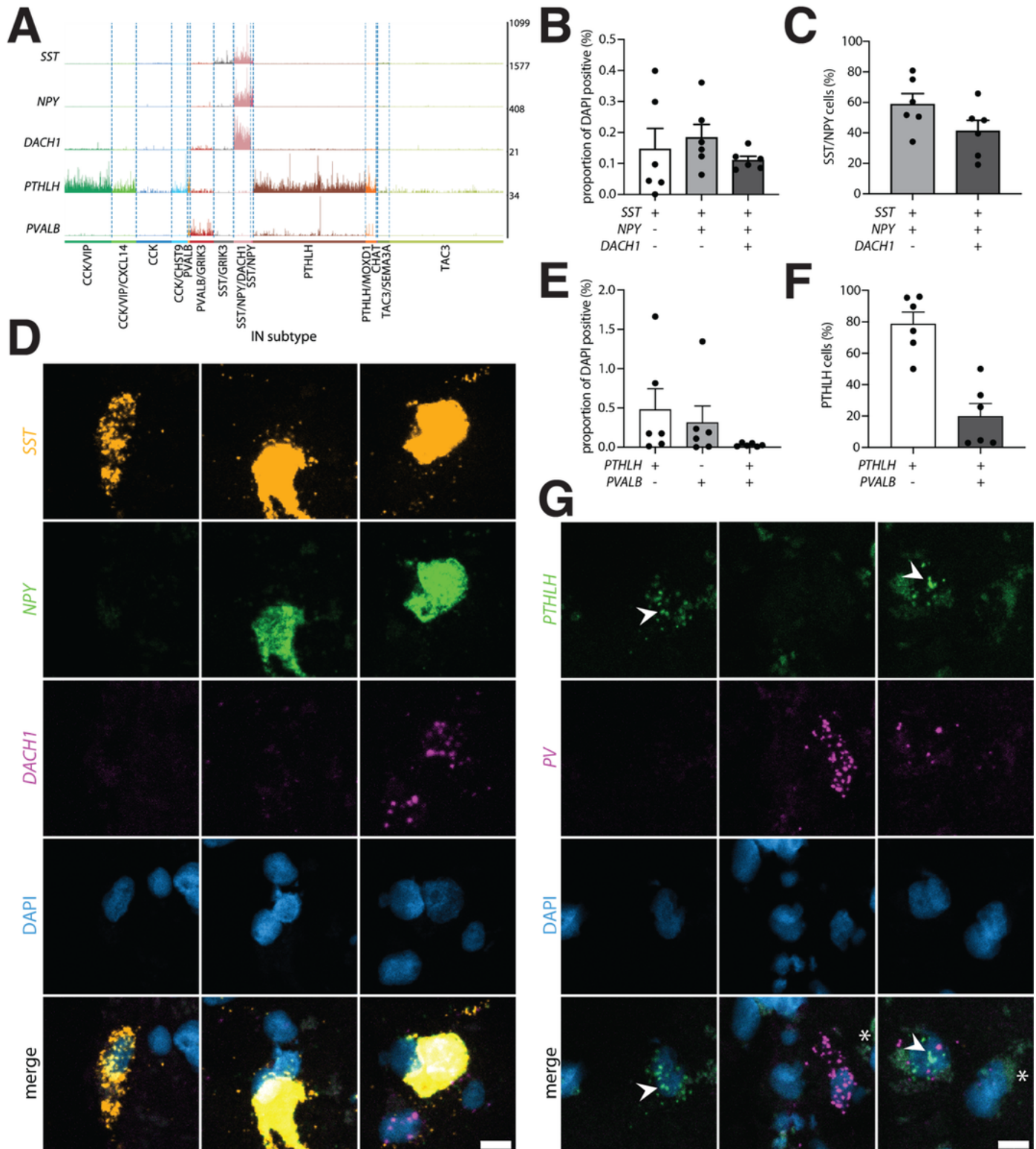


Figure 2

Validation using quantitative fluorescence *in-situ* hybridization confirms the existence of novel interneuron subclasses in the putamen. **A.** Trackplot depicting raw UMI counts per nucleus for *SST*, *NPY*, *DACH1*, *PTHLH*, and *PVALB* in caudate and putamen. **B.** Proportion of cells positive for *SST*, *SST* and *NPY* or *SST*, *NPY*, and *DACH1* based on the total number of cells identified per donor (N = 6, putamen). **C.** Proportion of *SST* and *NPY* double-positive cells negative or positive for *DACH1* (N = 6, putamen). **D.** Representative images for (left) single-, (middle) double- and (right) triple-positive cells from the same donor, scale bar 10 μm . **E.** Proportion of positive cells for *PTHLH*, *PVALB*, or *PTHLH* and *PVALB* based on the total number of cells identified per donor (N = 6, putamen). **F.** Proportion of *PTHLH* positive cells negative or positive for *PVALB* (N = 6, putamen). **G.** Representative images for (left and middle) single- or (right) double-positive cells from the same donor. White arrows indicate spot signal for *PTHLH*, asterisks mark autofluorescence due to lipofuscin, scale bar 10 μm .

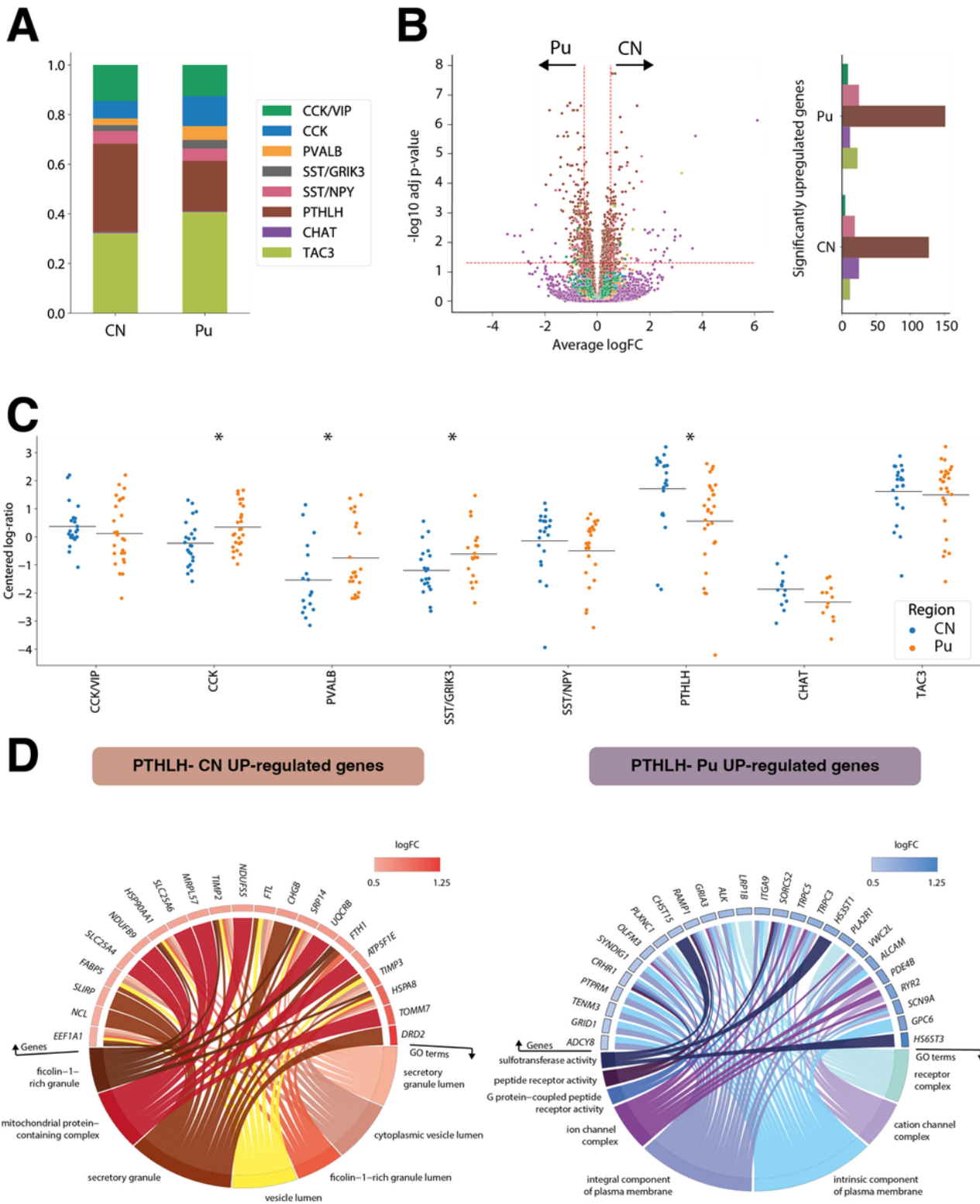


Figure 3

Striatal interneuron classes exhibit region-specific differences. **A.** Barplot illustrating the different proportions of interneuron subclasses in CN and Pu. **B.** (left) Volcano plot showing differentially expressed genes (DEGs) for each subclass. DEGs with an adjusted p-value < 0.05 and an average logFC greater than 0.5 were selected. (right) Number of significantly upregulated genes per interneuron class on each region. **C.** Scatter dot plot representing the compositional analysis estimated by centered log-ratio

method with significant compositional differences between CN and Pu in CCK, PTHLH, PVALB, and SST/GRIK3 interneurons. **D.** GO-term enrichment analysis of up-regulated genes in PTHLH subpopulation in CN and Pu. GO circle plot illustrating enriched terms (adjusted p-value < 0.05) with their respective enriched genes along with the logFC of these genes. *p < 0.05. CN, caudate nucleus; Pu, putamen.

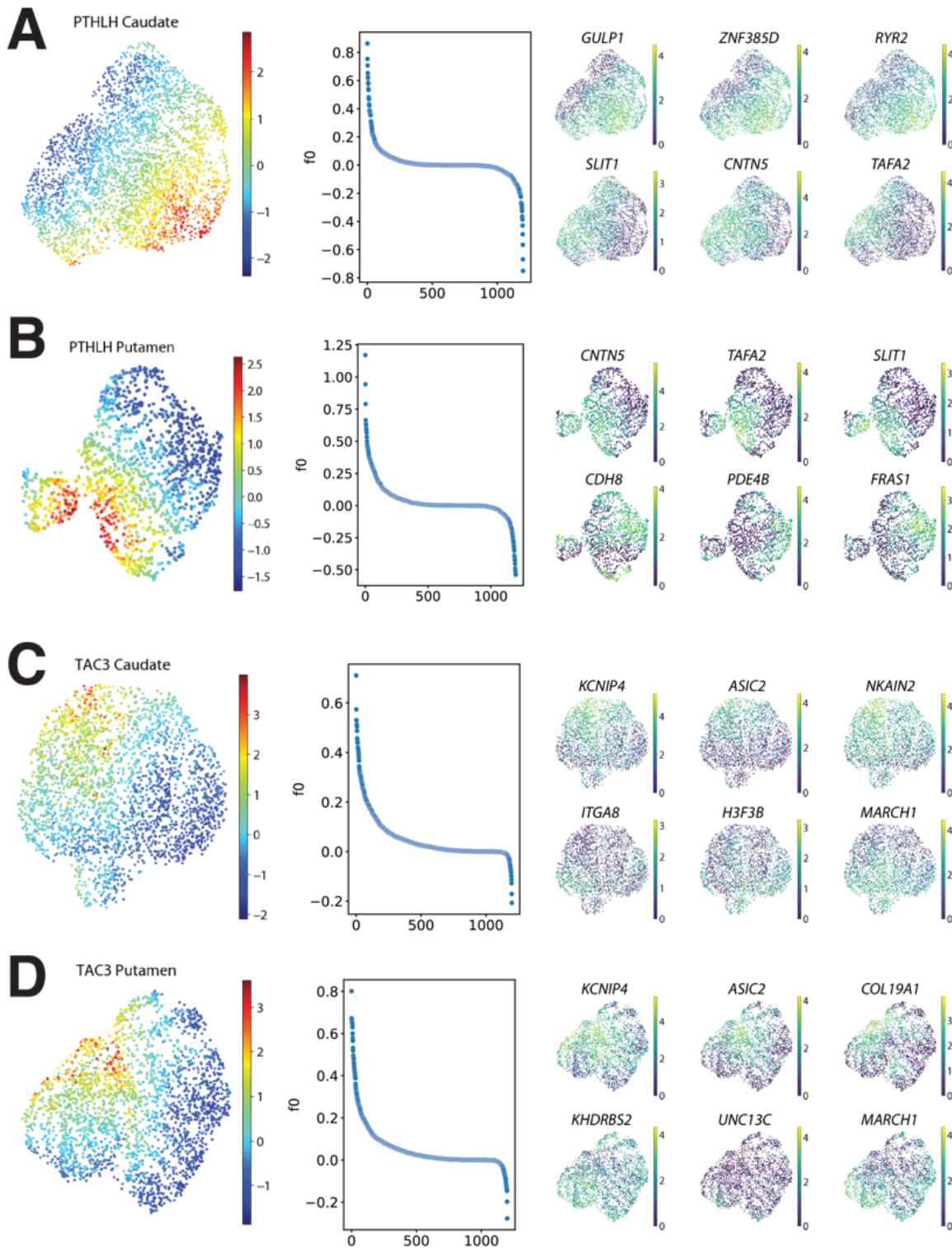


Figure 4

Factor analysis within interneuron subtypes. A. (left) UMAP projection of the PTHLH subclass from the CN, colored by the value of the factor obtained by running factor analysis. (middle) Factor weights associated with each gene. (right) UMAP projection of the PTHLH subclass interneurons colored by the expression level of (top row) the genes with the top three (bottom row) and bottom three weights on the factor. **B, C and D.** (left) Factor values, (middle) weights distributions and (right) expression of genes with largest contributions to the factor obtained for the PTHLH subclass from the Pu, the TAC3 subclass from the CN, and the TAC3 subclass from the Pu, respectively. CN, caudate nucleus; Pu, putamen.

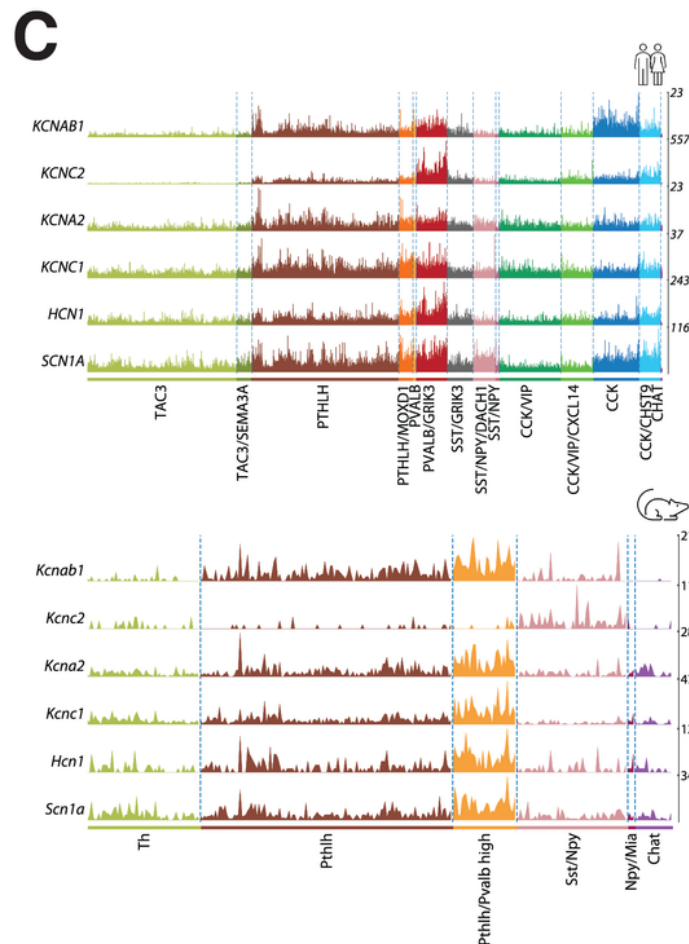
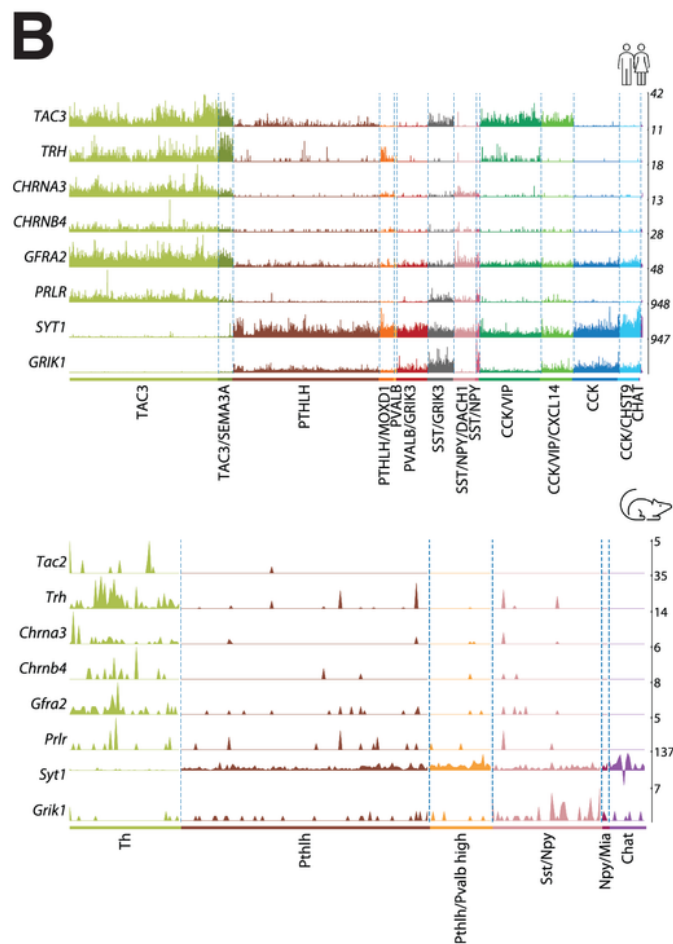
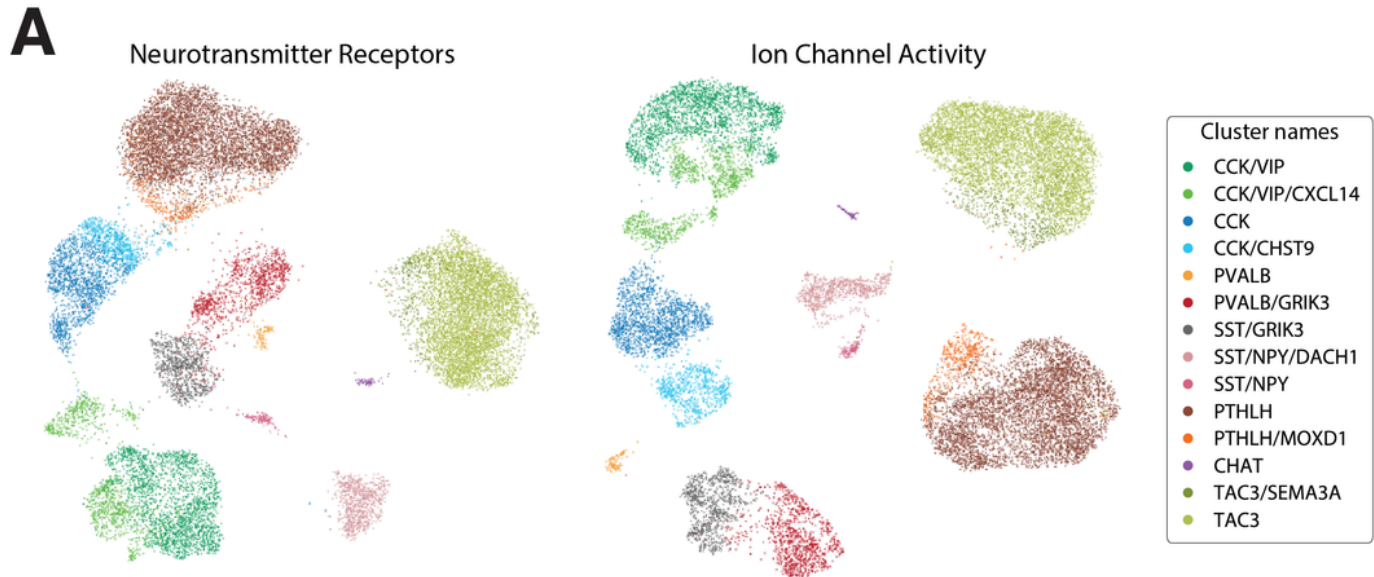


Figure 5

Comparison of striatal interneuron subclasses between mouse and human. A. (left) UMAP projection of the interneuron nuclei using expression data restricted to neurotransmitter receptor genes. (right) UMAP projection of the same data restricted to the genes annotated with the molecular function “ion channel activity” (GO:0005216). Colored based on the interneuron classification established before. **B.** (top) Expression values of genes suggesting parallelisms between the TAC3 subclass in the present human dataset and (bottom) the Th interneurons in the mouse striatum described by Muñoz-Manchado et al.². **C.** (top) Expression values of genes related to the fast-spiking phenotype in this human striatal dataset vs. (bottom) the striatal mouse dataset from Muñoz-Manchado et al.²

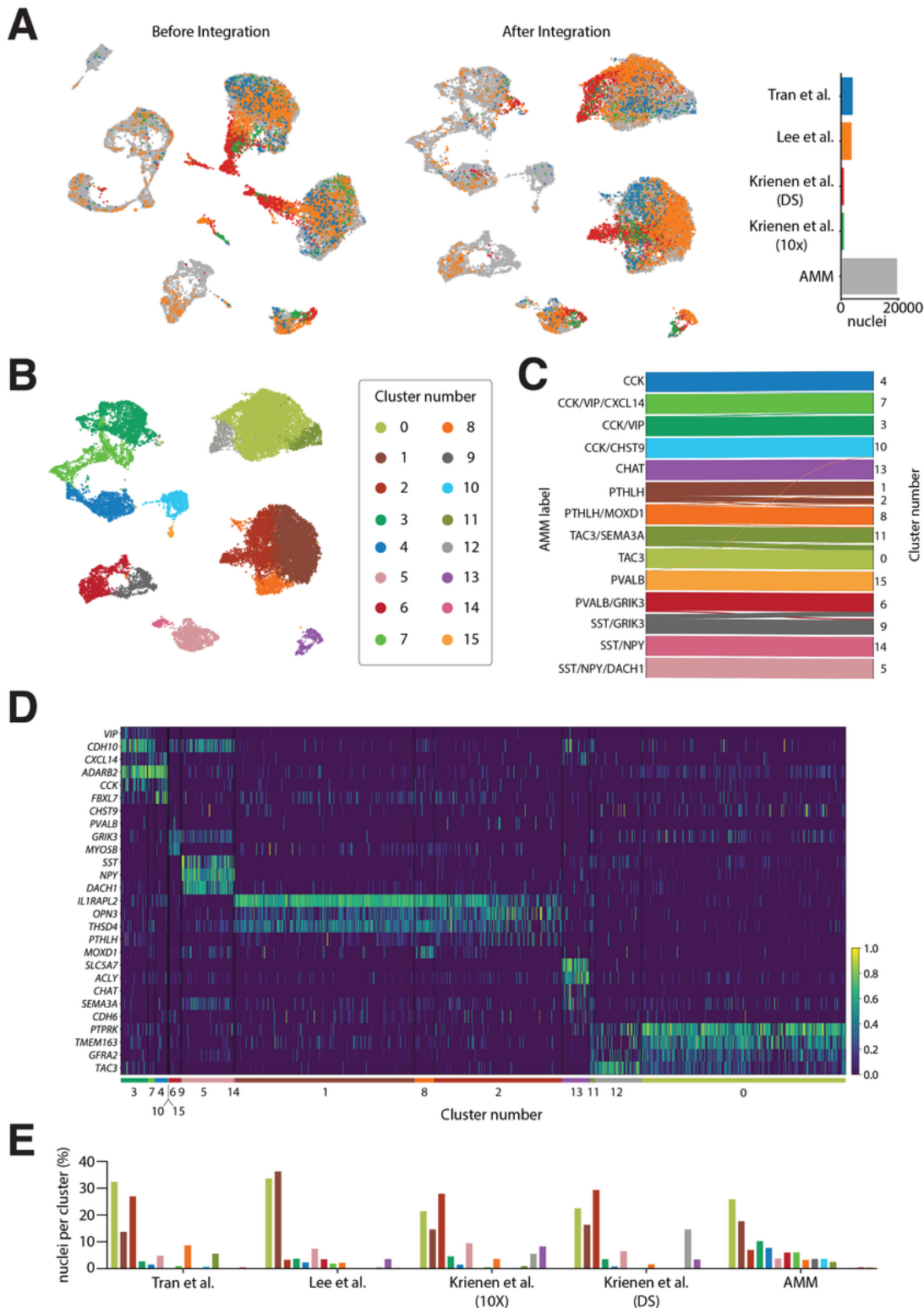


Figure 6

Interneuron taxonomy is consistent across multiple human striatal snRNA-seq datasets. **A.** (left) UMAP projection of interneuron nuclei from five different datasets before and (middle) after integration with scVI. (right) Barplot indicating the total number of nuclei from each dataset. **B.** UMAP projection of the integrated data colored by cluster. **C.** Shankey diagram relating the labels of the nuclei in the AMM dataset to the clusters obtained on the integrated data. Only assignments with more than 1% of the cells

of each subclass are shown. **D.** Normalized expression of interneuron subclass marker genes on the integrated public datasets (excluding our own). **E.** In each dataset (*x* axis), each bar represents the percentage of all interneuron nuclei detected in that dataset (*y* axis) that belongs to a specific cluster color-coded as in C.

Supplementary Files

This is a list of supplementary files associated with this preprint. Click to download.

- [supplementarytableGarmaetal.xlsx](#)
- [SupplementaryFigures.docx](#)